# Dynamical Diversity in Conductance-Based Neuron Response to kilohertz Electrical Stimulation

J. G. Polli[1,2], F. Kolbl [2], P. Lanusse [2], and M. G. E. da Luz [1]

[1] *Departamento de Física, Multidisciplinary Laboratory for Modeling and Analysis of Data in Complex Systems (MADComplex), Núcleo de Modelagem e Computação Científica-Centro Inerdisciplinar de Ciência, Tecnologia e Inovação, Universidade Federal do Paraná, 81531-980, Curitiba-PR, Brazil and*

[2] *IMS Lab, CNRS UMR 5218, Univ. Bordeaux, Bordeaux INP, Talence, France*

(Dated: August 26, 2025)

Brain neuron networks are notably rich in structure and functioning, consequently rather diverse in their dynamical feedback to stimuli. Thus, accurately characterizing the neural response to external signals is a crucial first step in understanding these networks, which conceivably could enable neuroscience and medical applications. In particular, kilohertz (kHz) neuronal electrical stimulation is a technique capable of inducing behaviors and drives unseen in more conventional lower frequency ranges. This fact could be used in the development of neuromodulation therapies for neurological pathologies, e.g., Deep Brain Stimulation (DBS). Here, we investigate neuronal response and excitability of conductance-based models to kHz frequencies stimulation in a still unexplored parameter space region. We show that the dynamics exhibited by the paradigmatic Hodgkin-Huxley model under kilohertz stimulation is highly diverse, displaying from regular spiking to chaotic behavior, as well as regions of complete activity suppression. By extending the analyses to models of mammalian central nervous system regions we show that, despite presenting similar low-frequency dynamics, such neurons tend to respond rather differently under kilohertz. Further, based on dynamical markers, we propose a method for systematically mapping these behaviors on a stimulation parameter space. These results establish a quantitative framework for ultra-high-frequency neuromodulation protocols, paving the way for future computational neuroscience approaches to stimulation-based procedures.

Keywords: Neuronal dynamics, chaos, feed-forward control, Hodgkin-Huxley, mammalian neurons

## I. INTRODUCTION

### A. Context and motivations

Biological neurons constitute paradigmatic examples of complex dynamical systems, comprising large cellular variability interlinked through nonlinear interactions [1]. Indeed, processes occurring at single neuron level give rise to neural circuit phenomena (e.g., rhythmic cycles, synchronization, firing patterns, etc) ultimately emerging in brain functions, such as behavior, memory, and cognition [2, 3]. However, alterations in structural and functional connectomics of neural circuits may disrupt this emergent complexity, eventually leading to neurological pathologies [4]. In these cases, therapeutic approaches broadly known as neuromodulation [5] rely on chemical, mechanical, and electrical interventions to reorient the dysregulated neural structures. Despite the prevalence of pharmaceutical treatments, its adverse effects [6] and limitations have motivated further developments of the latter type of stimulation.

The usage of electrical signals to intervene in neural systems requires a proper (and ideally general) framework, based on control theory of dynamical systems, aimed to complex [7] and nonlinear networks [8]. This might be achieved by assuming neural entities as high-dimensional nonlinear dynamical systems, such that brain states can be defined as attractors in the systems phase space [9–12]. Particularly, healthy and diseased brain states can also be associated with specific attractors [13, 14], whose transition takes place through bifurcation phenomena [15]. Therefore, in very broad terms, therapeutic control strategies would correspond to drives from pathological to healthy attractors [16–20]. So, to understand the response of neuronal models to external forcing is crucial to bridge theoretical and clinical therapeutic procedures [21–24].

Actually, neuronal electrical stimulation demonstrates clinical efficacy in diverse contexts. These include counteracting chronic pain [25], visual impairment [26], restoring sensory information [27], and alleviating neurodegenerative disease symptoms [28]. Typically, electrical stimulation of nervous system are based on feed-forward control, i.e., without feedback, delivering squared-shaped pulses of frequency within the range of physiological firing-rate of neurons to trigger a cell response. Also, stimulation is often delivered at 130 Hz, termed High Frequency (HF) in the literature [29]. Remarkably, HF has been successfully applied in the form of Deep Brain Stimulation (DBS) for managing conditions such as Parkinson's Disease (PD) [30], Obsessive-Compulsive Disorder (OCD) [31] and Alzheimer's Disease (AD) [32]. Nevertheless, the precise action of HF sparkling in brain circuits remains under debate [33].

Mostly based on empirical results, it has been determined that fine tuning of stimulation parameters — including waveform and frequency — may enhance therapeutic efficacy, specially when integrated with feedback control [34]. Modified pulse shapes are shown to reduce side effects in the case of epilepsy therapies [35]. Similarly, exploration of distinct frequency intervals has proven effective. For example, stimulation in the kilohertz range, termed Ultra-High Frequencies (UHF), applied in Peripheral Nerve System (PNS) blocks action potential propagation [36] and reduces post-amputation pain by inhibiting afferent nociceptive signals [37]. Although the precise mechanisms underlying kilohertz-induced neural block are not fully understood, exposing neurons to such frequencies has been associated with sodium channels inactivation [38], thereby mimicking inhibitory effects. Notably, computational modeling of kilohertz-frequency stimulation in

PNS — grounded in the Hodgkin-Huxley cable equation approach [39] — have successfully reproduced *in silico* [40–42] key phenomena observed *in vivo* [43–45]. These models now allow the design of UHF therapeutic protocols for neuromodulation of PNS [46].

Regarding the Central Nervous System (CNS), early studies indicated that UHF DBS lacked clinical efficacy [47, 48], primarily due to intrinsic low-pass filtering properties of neuronal membranes [49]. However, a recent trial of 10 kHz DBS on PD patients showed significant improvement in motor symptoms and verbal fluency, while reducing stimulation-induced side effects [50]. CNS neuromodulation fundamentally differs from PNS stimulation given the dense inter-connectivity and cellular diversity of the networks involved. Current literature addressing CNS response to UHF kilohertz frequency stimulation remains limited [51–55]. Computational studies using conductance-based model of Subthalamic Nucleus (STN) — a conventional PD DBS target — evaluated spike-suppression traits [51]. Experimental evidence revealed the response of hippocampal cells to be diverse [52] and hyperpolarized [53], while Retinal Ganglion Cells (RGCs) presented correlation between depolarization and spike-suppression both *in vitro* and *in silico* conductance-based models [54]. Notably, the sole *in-vivo* assessment of UHF neural responses in awake mice (1 kHz stimulation in hippocampal CA1) pointed to robust cellular and network-level modulation [55]. These findings indicate diverse electrophysiological responses to UHF in CNS tissues, highlighting therapeutic potential. Thus, comprehensive investigation on cell-type specific mechanisms is key to elucidate UHF neuromodulation principles in brain networks.

### B. Goals and overview of the general approach

In the present study, we comprehensively investigate the CNS dynamical responses to UHF stimulation supposing a class of *conductance-based neuron* models. In certain contexts [54], this kind of description has been validated in the kilohertz range through direct comparisons with *in vitro* measurements of quantities such as spike-counting and average membrane polarization. These positive findings suggest that conductance-based theoretical constructions can adequately portray some aspects of biological neurons, helping to answer the questions raised in the preceding section.

Hence, we propose a general scheme, grounded on dynamical systems, to characterize and map the UHF-induced dynamics in single-cell models of typical neuromodulation targets. The suggested approach seeks to develop a framework to identify the temporal evolution underlying neuronal responses to UHF. Even if restricted to individual neurons and periodic waveforms, this fundamental study may guide the development of cutting-edge experimental setups — such as those in [52–55] — and possibly supporting next-generation neuromodulation strategies.

All the neurons modeled here are assumed spatially structureless, Fig. 1(a), with a current clamp represented by the external periodic forcing term

$$I_{\text{stim}}(t) = I_0 + A_{\text{stim}} \sin[2\pi f_{\text{stim}} t] \tag{1}$$

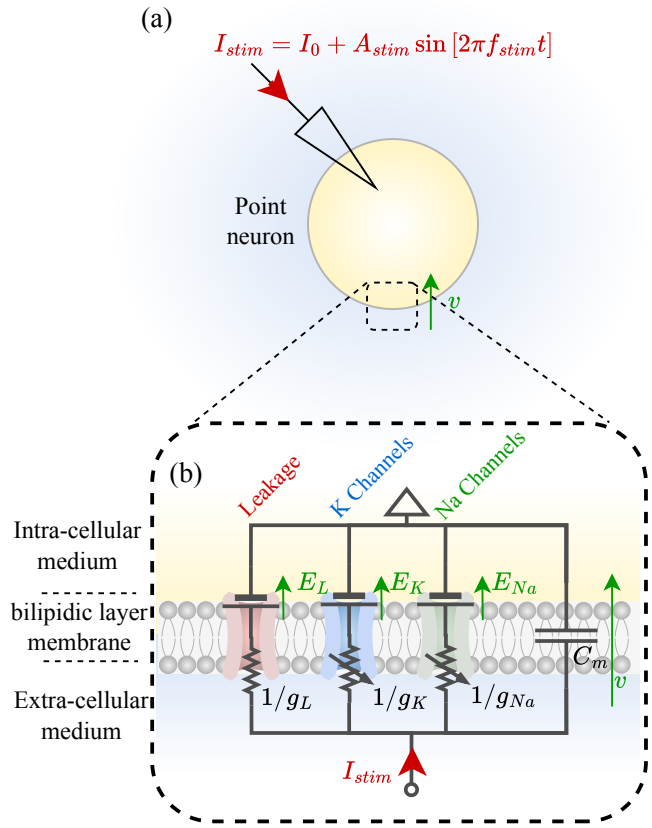


FIG. 1. (a) Schematic representation of a point (spatially structureless) neuron stimulated by a current clamp comprising DC and sinusoidal components. (b) Detailed view of the Hodgkin-Huxley (HH) modeling of bilipidic neuronal membrane, where the stimulation current is injected into a conductance-based circuit. The bilipidic neuronal membrane is described as a capacitor of capacitance $C_m$ in parallel with $Na^+$, $K^+$ and leakage ionic channels, controlled by specific resting potentials and resistors, with dynamical conductances.

Above, $I_0$ is the direct current (DC) stimulation and $A_{\text{stim}}$ and $f_{\text{stim}}$ are the amplitude and frequency of the sinusoidal stimulation. For the UHF response, we focus on supraphysiological stimuli, i.e., on the regime $f_{\text{stim}} > f_{\text{spk}}^{\max}$, where $f_{\text{spk}}^{\max}$ is the maximum firing-rate achieved under DC stimulation, namely, $I_{\text{stim}} = I_0$ (refer to Fig. 2(a) and the discussions in Sec. II A).

First, we consider the Hodgkin-Huxley (HH) model [39] for probing neuron response under supraphysiological stimulation. The HH, a conductance-based dynamical system of the giant squid axon, describes the membrane potential $v(t)$ via a nonlinear system of ordinary differential equations. Its equivalent circuit, Fig. 1(b), models the neuronal membrane as a capacitor — with membrane capacitance per unit of surface area $C_m$ (in $\mu\text{F}\cdot\text{cm}^{-2}$) — in parallel with three resistive branches. These are ionic channels, related to leakage ($L$), potassium ($K$), and sodium ($Na$), with respective voltage-dependent conductances $g_L, g_K, g_{Na}$ and constant reversal potentials $E_L, E_K, E_{Na}$. Further details are provided in the Appendix A 1. While the HH-model has been extensively explored, revealing, e.g., bifurcation phenomena under

DC clamp [56–59], and advanced coding properties under more complex inputs [60], in the UHF regime, studies are limited [51, 54]. Here we address such model for kilohertz frequency stimulation, investigating the resulting trajectories, the stroboscopic bifurcation map, spectral components, Lyapunov exponents and identifying distinct dynamical regimes in the parameter space.

A relevant technical aspect, likewise important for the understanding of neural functioning is the following. The HH model is four-dimensional, of variables $v$, $m$ (sodium activation) and $h$ (inactivation) and $n$ (potassium) gating. Usually in the literature, the system for HF is reduced to three or even two dimensions [61–63] by simplifying or eliminating the sodium dynamics. Nonetheless, sodium channels play a critical role in the propagation block mechanism observed in PNS under UHF regimes [36, 64]. So, we solve the full model for proper analyzes, but also discuss reduced variants for comparisons.

Second, we address generalizations of the standard HH, discussing the response of CNS mammalian conductance-based models under kilohertz frequency stimulation. These include cortical [65], hippocampal (pyramidal excitatory [66] and basket inhibitory cells [67]), subthalamic nucleus (STN), globus pallidus (GPe) [68], and retinal ganglion cells (RGCs) [69]. Performing Lyapunov, trajectory and phase-space diagnoses in the same manner as for the HH model, we examine the map of emergent dynamics in the supraphysiological stimulation parameter space. Our findings quantify cell-type attractors and provide neuromodulation tools for global parameter exploration, including hitherto unsurveyed regions.

## II. RESULTS

### A. The HH model diverse dynamical behaviors in the stimulation parameter space

In the present section we address the response of the HH-model to kilohertz electrical stimulation, examining the resulting trajectories and establishing a framework for frequency–amplitude parameter space exploration. But prior to that, we shall review some known dynamics of the HH-model under constant stimulation, i.e., $A_{\text{stim}} = 0$, with $I_{\text{stim}} = I_0$ for a varying $I_0$.

In Fig. 2(a) we show the evolution of Inter Spike Interval (ISI) and frequency of oscillation ($f_{\text{osc}} = 1/ISI$) as $I_0$ increases. In Fig. 2(b) we also show the bifurcation diagram with the stability of equilibrium and limit cycles for the extrema of the membrane potential $v$ at each value of $I_0$. The diagram elucidates the ISI and frequency behavior in Fig. 2(a). For $0 \leq I_0 < I_{H_1} = 9.775357\,\mu\text{A/cm}^2$, no spike is observed once the equilibrium is stable. For $I_0 = I_{H_1}$, a Subcritical Hopf Bifurcation occurs and the equilibrium becomes unstable, leading to a stable limit cycle with positive minimal frequency ($f_{\text{osc}}^{\text{min}} > 0$). Such threshold comportment classifies the HH neuron model as type-II [70], so opposed to type-I neurons which can fire at arbitrarily low frequencies. The spikes are sustained with increasing frequency as $I_0$ increases up to $I_0 = I_{H_2} = 154.5236\,\mu\text{A/cm}^2$, where a Supercritical Hopf Bifurcation reestablishes the stability of the equilibrium. The maximum attained frequency is $f_{\text{osc}}^{\text{max}} \sim 169\,\text{Hz}$, establishing an upper limit for the spiking frequency.

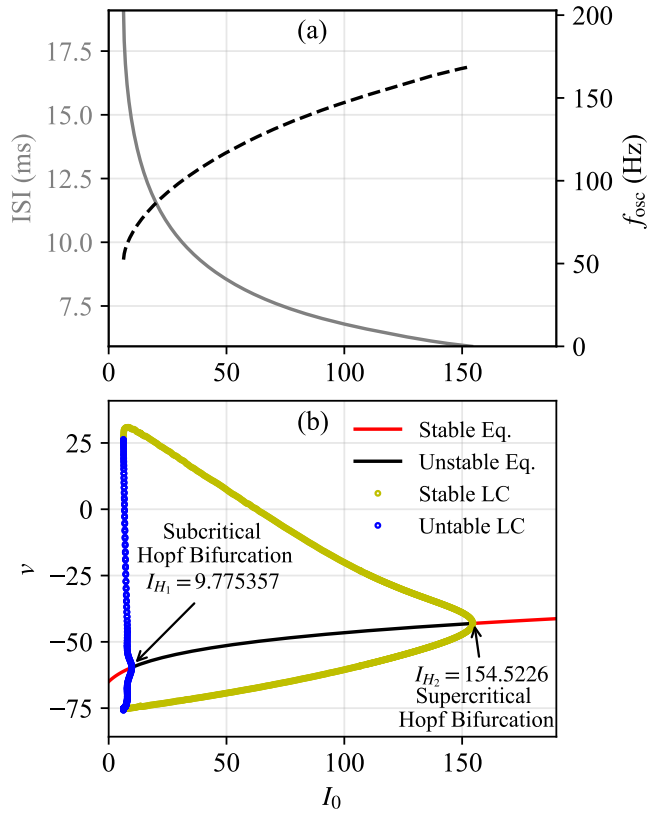


FIG. 2. (a) Inter-Spike Interval (ISI) and spiking frequency $f_{\text{osc}} = 1/ISI$, illustrating the class-II behavior of the HH model (i.e., displaying a positive minimal frequency). (b) Bifurcation diagram for the $I_0$ parameter, exhibiting stable and unstable equilibrium as well as stable and unstable limit cycles (LC). Their stability is shifted by Hopf bifurcations (Subcritical $I_{H_1} = 9.775357\,\mu\text{A/cm}^2$ and Supercritical $I_{H_2} = 154.5226\,\mu\text{A/cm}^2$).

#### 1. *Trajectories and spiking regimes*

For sake of comparison with prior works [51], for a given stimulation frequency $f_{\text{stim}}$ and amplitude $A_{\text{stim}}$ we can define the quantity

$$A = \frac{A_{\text{stim}}}{2\pi f_{\text{stim}} C_m}. \tag{2}$$

Physically, $A$ (expressed in mV) represents the amplitude of induced voltage in a purely capacitive membrane.

Consider now $A_{\text{stim}} > 0$ and $f_{\text{stim}} > f_{\text{osc}}^{\text{max}} > f_{\text{spk}}^{\text{max}}$. Figure 3(a)-(d) display examples of $v(t)$ for a neuron forced with $I_0 = 10.0\,\mu\text{A/cm}^2$ and stimulation frequency $f_{\text{stim}} = 1.0\,\text{kHz}$, for different amplitudes $A_{\text{stim}}$. For reference, under constant input $I_0 = 10\,\mu\text{A/cm}^2$ ($A_{\text{stim}} = 0\,\mu\text{A/cm}^2$) the equilibrium is unstable, since $I_{H_1} < 10\,\mu\text{A/cm}^2$, leading to periodic spiking

with period $T = 14.6\,\mathrm{ms}$ and spiking frequency of $f_{\mathrm{osc}} = 68.3\,\mathrm{Hz}$.

Figure 3(a) shows trajectories for stimulation with amplitude $A_{\mathrm{stim}} = 75\,\mu\mathrm{A/cm}^2$. From Eq. (2), this yields a voltage amplitude $A \approx 11.9\,\mathrm{mV}$. For this strength, the high-frequency components only modulate the underlying low-frequency spiking, consistently with averaging model predictions [51]. Figure 3(b) shows the dynamics for a higher stimulation amplitude, $A_{\mathrm{stim}} = 190\,\mu\mathrm{A/cm}^2$ ($A \approx 30.2\,\mathrm{mV}$). This elevates the spiking frequency — a trend potentially extrapolated from the DC stimulation bifurcation diagram (see Fig. 2). However, individual spikes now exhibit clear distortion from the forcing waveform. The resulting evolution no longer resembles DC stimulation behavior, nor locks harmonically with the stimulation frequency, although maintaining repetitive patterns. Notably, this dynamics matches *in vitro* experimental observations of RGCs under kilohertz-frequency stimulation [54]. Finally, Fig. 3(c)-(d) depicts dynamics at even higher stimulation amplitudes: $A_{\mathrm{stim}} = 410\,\mu\mathrm{A/cm}^2$ ($A \approx 65.3\,\mathrm{mV}$) and $A_{\mathrm{stim}} = 600\,\mu\mathrm{A/cm}^2$ ($A \approx 95.5\,\mathrm{mV}$), respectively. In Fig. 3(c), periodic spiking reemerges but with increased frequency and stronger modulation compared to Fig. 3(a). In Fig. 3(d), prominent spikes disappear, replaced by irregular oscillations with variable refractory periods. This variability aligns with known kilohertz-frequency stimulation effects [29]. Moreover, the trajectory irregularity resembles chaotic dynamics, a trend with desynchronization properties in networks [71]. We later quantify these qualitative observations employing Lyapunov analysis.

Periodicity in neural dynamics can be characterized by inter spike interval (ISI) measurements, requiring precise spike timing detection. However, as shown in Fig. 3(a)-(d) external forcing artifacts often difficult spike identification in membrane potential $v$ traces. Thus, we use the relative sodium conductance $g_{Na}/\overline{g}_{Na} = m^3 h$ — responsible for initializing depolarization in the HH model — as a reliable spike indicator (see Appendix A 1 for conductance details). In Fig. 3(e) we show an example of how the relative sodium conductance (left axis) compares with the membrane potential (right axis) for same stimulation parameters as in Fig. 3(d). While the membrane potential undergoes an unpredictable oscillatory comportment, the sodium relative conductance clearly distinguish active/inactive cellular states. So, we set a common conductance-based spiking threshold $m^3 h = 0.12$ (red dashed line in Fig. 3(e)), registering a spike when the relative conductance surpasses this value from bellow. This procedure is more reliable than to set membrane potential spiking thresholds (e.g. $v = 0\,\mathrm{mV}$, gray dashed line) which frequently registers double-crossings during forced oscillations.

Figure 3(f) displays a representative ISI diagram for $f_{\mathrm{stim}} = 1\,\mathrm{kHz}$ and stimulation ranging from 10 to $1000\,\mu\mathrm{A/cm}^2$. Vertical gray dashed lines mark the $A_{\mathrm{stim}}$ values of Fig. 3(a)-(d), ordered from left to right. For $A_{\mathrm{stim}} = 75\,\mu\mathrm{A/cm}^2$ and $A_{\mathrm{stim}} = 410\,\mu\mathrm{A/cm}^2$, a constant ISI indicates purely periodic behavior. For $A_{\mathrm{stim}} = 190\,\mu\mathrm{A/cm}^2$ a narrow band of ISI values suggests quasi-periodicity. Within 10–$350\,\mu\mathrm{A/cm}^2$, quasi-periodic and periodic regions alternate. Beyond $350\,\mu\mathrm{A/cm}^2$, ISI values distribute across multiple bands, presenting periodic windows that take turns with more complex patterns. For instance, at $A_{\mathrm{stim}} = 600\,\mu\mathrm{A/cm}^2$, ISIs range widely from 1 ms to 20 ms. A blow up into a region around $A_{\mathrm{stim}} = 560$ and $A_{\mathrm{stim}} = 640\,\mu\mathrm{A/cm}^2$ reveals complex ISI distributions, including bifurcation cascades and shading — characteristic of chaotic trajectories.

### 2. *Stroboscopic orbits diagram: classification of observable dynamics*

To inspect a wide range of possible dynamics for the forced HH neuron model, one can construct stroboscopic orbit diagrams by sampling trajectories at every $T_{\mathrm{strob}} = 1/f_{\mathrm{stim}}$ time intervals. Figure 4(a) shows such orbits for parameters $f_{\mathrm{stim}} = 1.25\,\mathrm{kHz}$, $I_0 = 0\,\mu\mathrm{A/cm}^2$ and stimulation amplitude ranging from 0 to $3000\,\mu\mathrm{A/cm}^2$. In the plots, background color highlight different ranges of spiking dynamics. Light lavender indicates absence of spikes ($A_{\mathrm{stim}} < 140.5\ \mu\mathrm{A/cm}^2$), while light red identifies spiking regions ($A_{\mathrm{stim}} > 140.5\ \mu\mathrm{A/cm}^2$). Within a spiking region we have periodic stroboscopic dynamics (i.e. subharmonic of the forcing frequency), where $P_k$ denotes a $k$-cycle stroboscopic orbit. As $A_{\mathrm{stim}}$ increases, the system shifts from $P_1$ (no-spike region) to a regime that alternates between aperiodic and periodic windows. Notably, within the spiking zone, periodic sectors appear in a sequence of decreasing periods $\{\ldots, P_5, P_4, P_3, P_2\}$. Extra examples of bifurcation diagrams are presented in the Supplemental Material (SM), Fig. S1 and Sec. S1.

In Fig. 4(b) we depict the corresponding maximum Lyapunov exponent (MLE) $\lambda$ (see Appendix A 3) for the trajectories in Fig. 4(a). The values are strictly negative before reaching the no-spike/spiking transition, indicating stable periodic trajectories. Along the transition, $\lambda$ switches between near-zero and strictly negative values. A more detailed inspection reveals near-zero $\lambda$ matching the aperiodic regions in the stroboscopic orbits diagram, enabling quantitative classification of such quasi-periodic (QP) trajectories. Positive $\lambda$'s, indicating chaotic dynamics, start around $A_{\mathrm{stim}} = 625\,\mu\mathrm{A/cm}^2$. Chaotic zones ($\lambda > 0$) alternate with periodic windows until the last observed aperiodic sector, before the $P_2$ region. To clearly distinguish periodic and aperiodic regimes, we computed the power spectral density (PSD) of trajectories (see Appendix A 3 for details). Fig. 4(c) presents the PSD results for the trajectories in Fig. 4(a). A prominent line at $f = 1.25\,\mathrm{kHz}$ corresponds to the forcing frequency. Notice that for all amplitudes, the forcing frequency acts as a modulation in the associated dynamics. Periodic regions $P_k$ exhibit $k$ distinct subharmonic peaks.

Figure 4(d) shows a zoom into the red-dashed rectangle in Fig. 4(a), detailing a reverse period-doubling cascade, well known to be a route to chaos [72]. This is consistent with the positive $\lambda$ values of this region in Fig. 4(b). Figure 4(e) represents the spectral profile for $P_4$ periodic dynamics, where 4 distinct peaks are observed in the PSD. Quasi-periodic zones ($\lambda \sim 0$) display multiple sharp dominant frequencies superimposed on the background frequencies, as exemplified in Fig. 4(f). In contrast, chaotic regimes ($\lambda > 0$) show

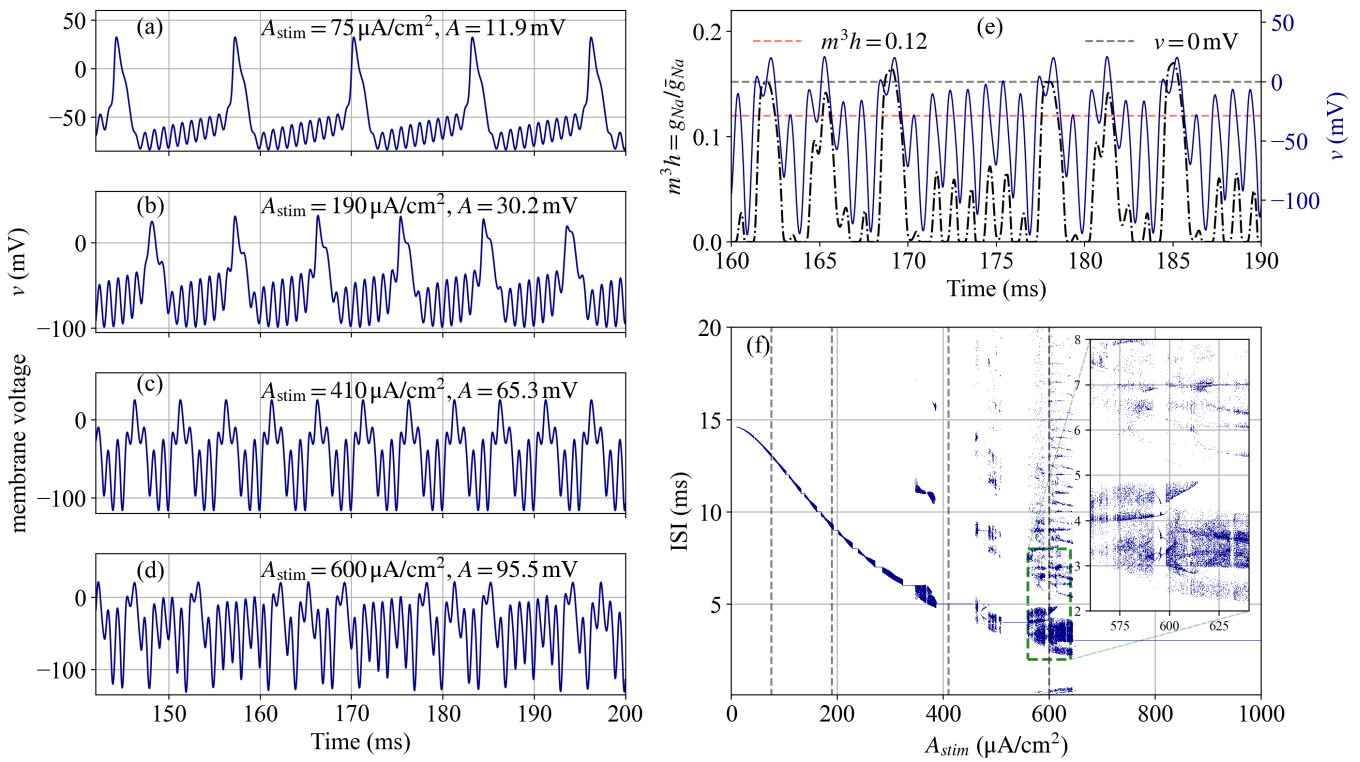


FIG. 3. Membrane potential time series, $v(t)$, and ISI (inter spike interval) for the Hodgkin-Huxley model stimulated with $I_0 = 10.0\,\mu\text{A/cm}^2$, $f_{\text{stim}} = 1.0\,\text{kHz}$ and representative values of $A_{\text{stim}}$. (a) The case $A_{\text{stim}} = 75\,\mu\text{A/cm}^2$ shows a periodic spiking behavior. (b) When $A_{\text{stim}} = 190\,\mu\text{A/cm}^2$, the spiking dynamics ceases to be periodic. (c) $A_{\text{stim}} = 410\,\mu\text{A/cm}^2$ leads to a periodic trajectory with ISI $\sim 5\,\text{ms}$, whereas (d) $A_{\text{stim}} = 600\,\mu\text{A/cm}^2$ displays an aperiodic spiking dynamics. (e) The sodium relative conductance $m^3h = g_{Na}/\bar{g}_{Na}$ along with the trajectory for $v(t)$ for $A_{\text{stim}}$ as in (d). The spiking thresholds $m^3h = 0.12$ and widely used $v = 0$ are indicated as references. (f) The ISI for $m^3h = 0.12$ taking as spiking threshold and the values of $A_{\text{stim}}$ ranging from $10\,\mu\text{A/cm}^2$ to $1000\,\mu\text{A/cm}^2$. The gray dashed lines marks the $A_{\text{stim}}$ value for the trajectories in (a)-(d). The inset zooms up a region where the ISI is far from periodic.

broadband noise without dominant peaks. This is illustrated in Fig. 4(g), where besides the forcing frequency, no distinct peaks emerge above the background noise.

Figure 4 is computed for $I_0 = 0\,\mu\text{A/cm}^2$ and $f_{\text{stim}} = 1.25\,\text{kHz}$. In Sec. S1 of the SM, we display stroboscopic bifurcation diagrams for additional combinations of DC currents, $I_0 = 0, 5, 10\,\mu\text{A/cm}^2$, and stimulation in the kilohertz range, i.e., $f_{\text{stim}} = 1, 1.25, 2.75, 5\,\text{kHz}$. We observe that the amplitude value at which there is a transition (from no-spike to spiking) decreases as $I_0$ increases. If $I_0 > I_{H_1}$, the no-spike phase disappears, as expected from the analysis in Fig. 2.

In total, we found four distinct responses of the HH model to kilohertz frequency in the frequency–amplitude parameter space. (i) Non-Spiking (NS) dynamics: taking place below a threshold stimulation amplitude, $I_0 < I_{H_1}$. (ii) Periodic subharmonic dynamics: membrane potential oscillations phase-lock with a subharmonic of $f_{\text{stim}}$, exhibiting constant spiking frequency, period-$k$ ($P_k$) stroboscopic dynamics, $\lambda < 0$, and $k$ subharmonic peaks in the PSD. (iii) Quasi-Periodic (QP) dynamics: aperiodic trajectories with $\lambda \sim 0$ that bridge consecutive $P_k$ and $P_{k-1}$ periodic windows. (iv) Chaotic dynamics: displaying aperiodic trajectories with $\lambda > 0$. It emerges primarily through period-doubling cascades.

Actually, a fifth comportment also occurs with non-zero DC current, $I_0 \neq 0\,\mu\text{A/cm}^2$. For constant stimulation, the HH model exhibits periodic oscillatory behavior between Hopf bifurcations ($I_{H_1} < I_0 < I_{H_2}$). Figure 5 shows a stroboscopic orbits diagram for $I_{H_1} < I_0 = 20\,\mu\text{A/cm}^2 < I_{H_2}$ and $f_{\text{stim}} = 5\,\text{kHz}$. A first region with multiple spikes can be observed until a threshold of $A_{\text{stim}} = 497\,\mu\text{A/cm}^2$. For $A_{\text{stim}} > 497\,\mu\text{A/cm}^2$, the membrane voltage turns into a non-spiking $P_1$ behavior, with values typical of hyperpolarization. As discussed in [51], we call this trend spike-suppression (SS), since the application of UHF represses neural activity (we mention we have reproduced the result in [51] with identical parameters). Importantly, SS differs from NS: the DC current alone would elicit spiking, but here is the effect of sinusoidal stimulation that suppresses the spikes.

### 3. *Dynamical mapping of the parameter-space*

For the kilohertz-frequency range, we next qualitatively characterize the frequency-amplitude parameter space. In Fig. 6(a) we plot the MLE $\lambda$ for $A_{\text{stim}} \in [0, 7000]\ \mu\text{A/cm}^2$, $f_{\text{stim}} \in [0.4, 3.5]$ kHz and DC current $I_0 = 0$. The ex-

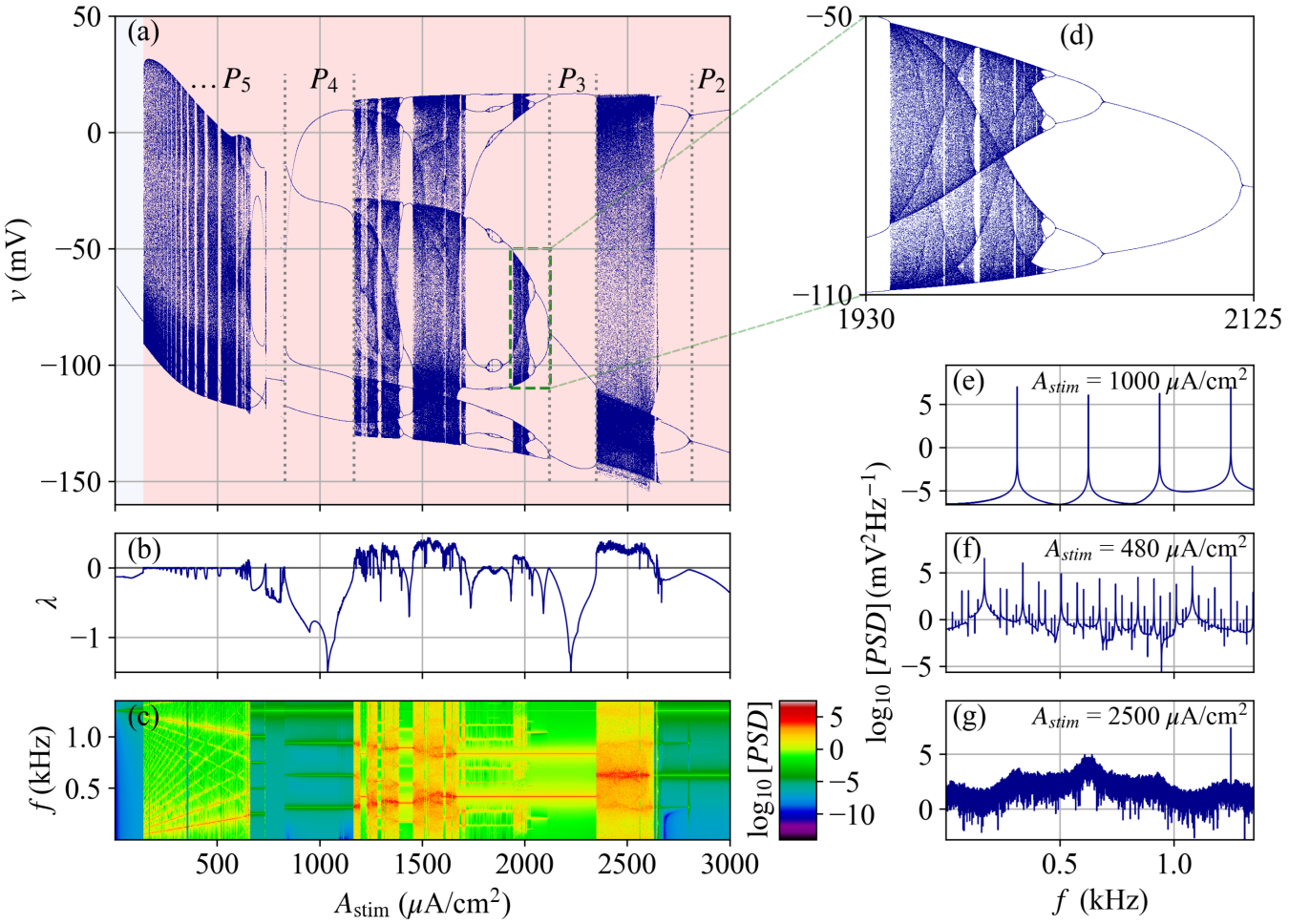


FIG. 4. Dynamical transitions and spectral features of the kilohertz-frequency stimulated HH neural model for $f_{\text{stim}} = 1.25\,\text{kHz}$ and $I_0 = 0\,\mu\text{A/cm}^2$. (a) Stroboscopic orbits diagram of the membrane potential $v$ versus stimulation amplitude $A_{\text{stim}} \in [10, 3000]\,\mu\text{A/cm}^2$. Background color indicates no-spiking (white) and spiking (light red) dynamics. Vertical dotted lines delimit examples of subharmonic zones ($P_k$ for $k$ the stroboscopic period). (b) Maximum Lyapunov exponent $\lambda$ for the same parameter range. (c) Logarithm PSD showing distribution of spectral components. (d) A blow up of the stroboscopic orbit diagram of (a) in the interval $A_{\text{stim}} \in [1930, 2125]\ \mu\text{A/cm}^2$ showing a reverse period-doubling bifurcation route to chaos. Spectral profiles for three regimes, (e) quasi-periodic ($\lambda \sim 0$) for $A_{\text{stim}} = 500\,\mu\text{A/cm}^2$, (f) $P_4$ subharmonic for $A_{\text{stim}} = 1000\,\mu\text{A/cm}^2$, (g) chaotic ($\lambda > 0$) for $A_{\text{stim}} = 2500\,\mu\text{A/cm}^2$.

ponent $\lambda$ was calculated only for $A < 475$ mV (see Eq. (2)), thus avoiding unphysiological hyperpolarization regimes. Chaotic regions ($\lambda > 0$) occupy dense bands for stimulation frequencies below 3 kHz and amplitudes from few tens to about $6500\,\mu\text{A/cm}^2$. Moreover, these bands arise within $40\,\text{mV} < A < 425\,\text{mV}$, demarcated by red (40 mV) and yellow (425 mV) dashed lines in Fig. 6(a).

We further classify the response of the HH model to each frequency-amplitude combination using an algorithm described in Appendix A 4. It identifies the five behaviors specified in Sec. II A 2, namely, chaotic, quasi-periodic (QP), periodic ($P_k$), no-spiking (NS) and spike-suppression (SS). Figure 6(b) shows the resulting dynamical map for $I_0 = 0$ (related to Fig. 6(a)). As previously described, chaotic zones form bands. QP zones are limited to a region in the bottom-left part of the map, vanishing above 1.75 kHz and amplitude $\sim 1000\,\mu\text{A/cm}^2$. NS are present in the top-left map region, corresponding to lower induced membrane voltage amplitudes. SS is absent once $I_0 = 0$ prevents spiking without sinusoidal forcing. Periodic regions are scattered over a great fraction of the parameter space, with higher-period orbits embedded within QP and chaotic zones. All periodic regions tend to $P_2$ as the induced membrane potential amplitude $A$ increases, leading to a $P_2$ dominance for $A > 475\,\text{mV}$. Furthermore, transitions are observed between distinct regimes (in the functional mapping, Fig. 6(b)): QP $\leftrightarrow$ NS (bottom-left), NS $\leftrightarrow P_k$ (top left), QP$\leftrightarrow P_k$ (bottom left), $P_k \leftrightarrow P_j$ ($j \neq k$) and $P_k \leftrightarrow$ chaotic (center).

At this point, a brief summary of the previous results is in order. UHF stimulation induces diverse dynamical regimes in the HH model. Although the distribution of these regimes in the parameter space is somehow involved, extended regions of

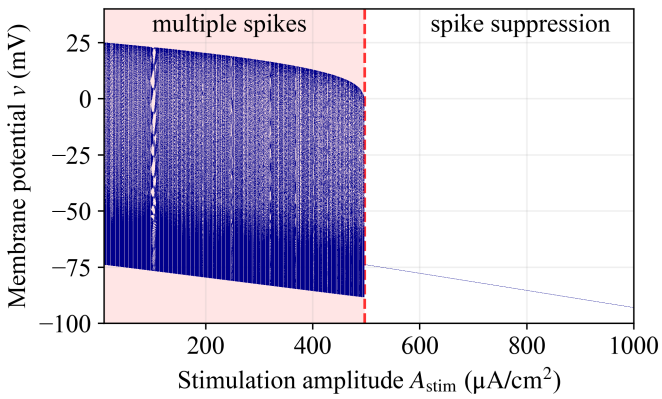


FIG. 5. Stroboscopic plot for $f_{\text{stim}} = 5\,\text{kHz}$ and $I_0 = 20\,\mu\text{A/cm}^2$, illustrating spike-suppression as $A_{\text{stim}}$ increases. At small amplitudes, spikes are present until a threshold (here of $497\,\mu\text{A/cm}^2$). Beyond it, no spike is triggered and the membrane potential tends to decrease fairly linearly with $A_{\text{stim}}$, indicating that the cell is hyperpolarized.

uniform behavior are present. The density and dimensionality of the chaotic and periodic regions are still open questions (and a problem which hopelly we will address in a forthcoming contribution). Nonetheless, they are relevant for targeting specific neuronal responses in neural engineering procedures, see the Discussion section.

### B. Supra-physiologic stimulation effects on Na-channels dynamics

The mechanism of UHF stimulation in the PNS primarily involves Na-channel blocking, even though K-channels has not been fully excluded [36]. For CNS stimulation, the impact of supra-physiological frequencies on ionic channels remains elusive. Conductance-based models could clarify this key issue by elucidating how UHF stimulation modulates the dynamics of gating variables in ionic transport. Therefore, here we explore the action of UHF on dimension reductions of the HH model, where certain gating variables are removed.

As detailed in the Appendix A 1, the original 4D HH model — determining $v(t)$, $m(t)$, $h(t)$ and $n(t)$ — admits two distinct three-dimensional reductions; (1) a 3D $m$ reduction, replacing the $m$ variable by its steady-state $m_\infty$ value; and (2) a 3D $h$ reduction, eliminating the $h$ variable by supposing a linear relation between $h$ and $n$. (3) A third 2D reduction combines (1) and (2). Since the Na conductance depends on the quantity $m^3\,h$, the aforementioned simplifications directly impact on Sodium dynamics. However, these simplifications are widely used since they have a mildly influence on the model dynamics at low frequencies.

In (1)–(3), the bifurcation analysis for the DC stimulation ($A_{\text{stim}} = 0\,\mu\text{A/cm}^2$) preserves the succession of subcritical and supercritical Hopf bifurcation points. This leads to the same three dynamical comportment predicted by the full 4D HH model, i.e., a non-oscillatory behavior for $I_0 < I_{H_1}$, a limit cycle (spiking) behavior for $I_{H_1} \leq I_0 < I_{H_2}$, and a non-oscillatory (spike-suppression) behavior for $I_0 \geq I_{H_2}$. But as expected, the simplifications alter some parameters values, as those for $I_{H_1}$ and $I_{H_2}$ in Fig. 2(b) (refer to the Supplementary Material Section S2 for further details).

Figure 7(a-c) presents stroboscopic bifurcation diagrams for the full 4D, the 3D $h$ reduced and the 3D $m$ reduced HH models, respectively. All share the same forcing frequency ($f_{\text{stim}} = 1\,\text{kHz}$) and stimulation amplitude range ($A_{\text{stim}} \in [0, 700]\,\mu\text{A/cm}^2$). The systems exhibit a progression of periodic and quasi-periodic trends as $A_{\text{stim}}$ increases. Remarkably, the 3D $h$ reduced closely matches the sequence of periodic/quasiperiodic regimes of the 4D model, with significant deviations emerging only at high amplitudes. In contrast, the 3D $m$ reduced model displays important distinctions regarding these sequences, being much more sparse and displaying a different stimulation amplitude range.

Chaotic regimes ($\lambda > 0$) emerge in both 3D models (see Supplementary Material, Figs. S5 and S6). In the $h$ reduced case, chaos takes place for $A_{\text{stim}}$ in the interval 480–$500\,\mu\text{A/cm}^2$. As for the $m$ reduced version, the chaotic region arises in a narrow window around $A_{\text{stim}} = 135\,\mu\text{A/cm}^2$. The progression of periodic regimes shows fundamental differences among models. The 4D displays the characteristic sequence $\ldots P_5, P_4, P_3, P_2$ for higher stimulation amplitudes. In contrast, the sequence is truncated in the 3D models. For the $h$ reduced, $P_5$ transitions directly to SS, while for the $m$ reduced, the transition is from $P_4$ to SS.

The 2D model dynamics (see Supplemental Material, Fig. S7) somewhat resembles that of 3D $m$ reduced model, but with two relevant differences. First, chaotic regions are absent, which is consistent with theoretical expectations for systems of dimension $d < 3$. Second, the transitions occur from the periodic regime $P_3$ to SS.

Each gating variable $x$ (either, $m$, $h$ or $n$) does obey (see Eq. (A6) in Appendix A 1)

$$\dot{x} = \frac{x_\infty(v) - x}{\tau_x(v)}. \tag{3}$$

Above, as defined in Eq. (A5), $x_\infty(v)$ and $\tau_x(v)$ represent the voltage-dependent $x$ steady state value and time constant, respectively. Also, these quantities are related to sigmoidal-shaped rate functions $\alpha_x(v)$ and $\beta_x(v)$. Our findings demonstrate that the membrane voltage $v$ presents a non-trivial spectral response to UHF (see Fig. 4(d)). Moreover, because the steady-states $x_\infty(v)$ are monotonic functions of $v$, they inherit spectral components of $v$, including dominant components around $f_{\text{stim}}$.

The Eq. (3) further allows to interpret $x_\infty(v)$ as a forcing term for the $x$-gating variable dynamics. Additionally, it describes a low-pass filter, characterized by a voltage-dependent transition frequency (in Hertz)

$$f_x(v) = \frac{1}{2\pi\tau_x(v)}. \tag{4}$$

Assuming that $f_{\text{stim}}$ dominates the spectrum of $x_\infty$, then the gating variable exhibit two distinct regimes. When $f_{\text{stim}} \ll f_x$, the dynamics of $x(t)$ closely follows $x_\infty(v)$, so that $x \approx x_\infty(v)$ is a rather good approximation. Conversely, when $f_{\text{stim}} \gtrsim f_x$,

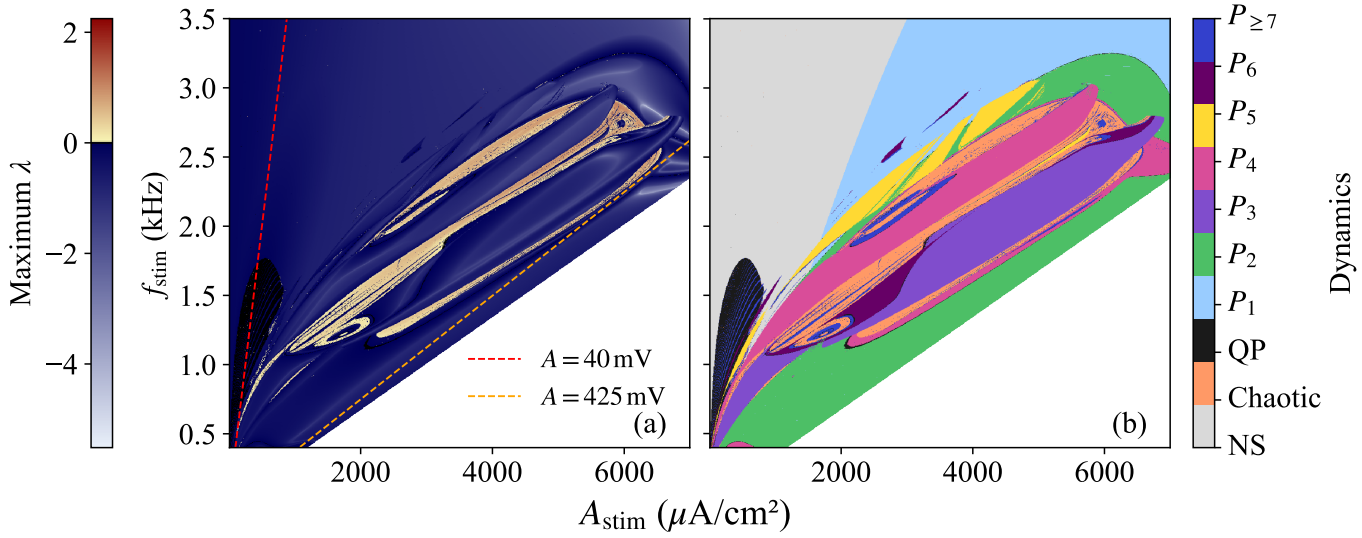


FIG. 6. (a) MLE map of the HH model for $f_{\text{stim}} \in [0.4, 3.5]$ kHz, $A_{\text{stim}} \in [100, 7000]$ $\mu$A/cm$^2$ and DC current $I_0 = 0$. Trajectories with $A > 475$ mV yield non-physiological hyperpolarization (besides being hard to numerically integrate). They correspond to the lower left part of the plots (white triangles). Red and yellow dashed lines delimit the region between 40 mV $< A <$ 425 mV. (b) Functional mapping of the HH model for the same parameter-space region of (a). It displays regions of non-spiking (NS), chaotic, quasi-periodic (QP) and subharmonic of periods $P_{k=1,\ldots,6}$ as well as $P_{k\geq 7}$. The algorithm to obtain the different regions is explained in the Appendix A 4.

the dynamics of $x(t)$ cannot track the external forcing, hence $x \approx x_\infty(v)$ is inaccurate.

For the 4D HH model, Fig. 7(d) depicts the evolution of the transition frequencies, Eq. (4), for typical values of $v$. For the $h$ and $n$ gating variables, the transition frequencies lie in the range of tens to hundreds of Hz. Therefore, under both HF ($\sim$ 130 Hz) or UHF stimulation, these variables operate in the regime $f_{\text{stim}} \gtrsim f_x$, invalidating assumptions like $h = h_\infty$ and $n = n_\infty$. In contrast, the transition frequency $f_m^{\text{min}}$ associated with the $m$ gating variable spans from around 317 Hz up to few kHz. Thus, for HF stimulation (or even lower) the simplification $m = m_\infty$ works well. But for kilohertz stimulation, the condition $f_m \ll f_{\text{stim}}$ no longer holds, invalidating the 4D to 3D reduction approach. Indeed, as shown by the stroboscopic bifurcation plots in Fig. 7(c), the 3D $m$ model fails to reproduce the characteristic dynamical structure of the full 4D HH under kilohertz stimulation. In this way, one can conclude that the influence of supra-physiological forcing is directly linked to Sodium channels, and in particular to their activation dynamics, governed by the $m$ gating variable.

Figure 7 (e) shows the average membrane potential $\langle v \rangle$ (see Appendix A 3) across a range of stimulation amplitudes and four different stimulation frequencies ($f_{\text{stim}} = 0.25, 0.5, 1.0, 1.25$ kHz) for the original 4D model. Such quantity, also referred to as *baseline*, has been modeled and experimentally measured in neural cells [54]. Our results align with previous findings: (i) for lower stimulation frequencies ($f_{\text{stim}} = 0.25$ kHz and 0.5 kHz), the baseline initially increases (depolarizes) at low amplitudes, then decreases toward resting potential and eventually hyperpolarizes as the amplitude increases; and (ii) for larger stimulation frequencies ($f_{\text{stim}} = 1.0$ kHz and 1.25 kHz), the baseline monotonically depolarizes with amplitude. Remarkably, (ii) corresponds to stimulation frequencies way above the minimal transition frequency of the $m$ gating variable, reinforcing the role of the Na activation dynamics in shaping the response to supra-physiological stimulation.

Lastly, Fig. 8 presents a stroboscopic bifurcation diagram in which $f_{\text{stim}}$ increases while the induced membrane potential amplitude $A$ is held constant so that $A_{\text{stim}}$ varies accordingly, refer to Eq. (2). When $f_{\text{stim}} < f_{\text{osc}}^{\text{max}} \sim 0.169$ kHz (blue dashed line in Fig. 8), the system exhibits a $P_1$ periodic response. This behavior remains unchanged as $f_{\text{stim}}$ crosses both $f_{\text{osc}}^{\text{max}}$ and $f_m^{\text{min}} = 0.317$ kHz (green dashed line in Fig. 8), with the neuron continuing to phase-lock with the stimulation. As the frequency is further increased, a sequence of transitions takes place: from $P_1$ to $P_4$, getting back to $P_2$, followed by QP dynamics, then $P_3$ and next going through a cascade of period doubling bifurcations, culminating into chaotic behavior. Although this does not account for the whole range of observed behaviors, it suggests that phenomena associated with UHF arise not only when $f_{\text{stim}} > f_{\text{osc}}^{\text{max}}$, but also for $f_{\text{stim}} \gg f_m^{\text{min}}$.

### C. Supra-physiologic stimulation effects on distinct mammalian neural models

The HH model has been extensively investigated for over fifty years, serving as a valuable neuron prototype to support and even benchmark more realistic studies (see, e.g., [51]). However, it was derived based on non-mammalian (squid) axon data, so not capturing the dynamical diversity of different brain structures. Therefore, to explore the effects of UHF in mammalian brain — trying to be in line with certain known important processes [51, 54] — we performed a mapping of behaviors induced by kilohertz stimulation discussing models

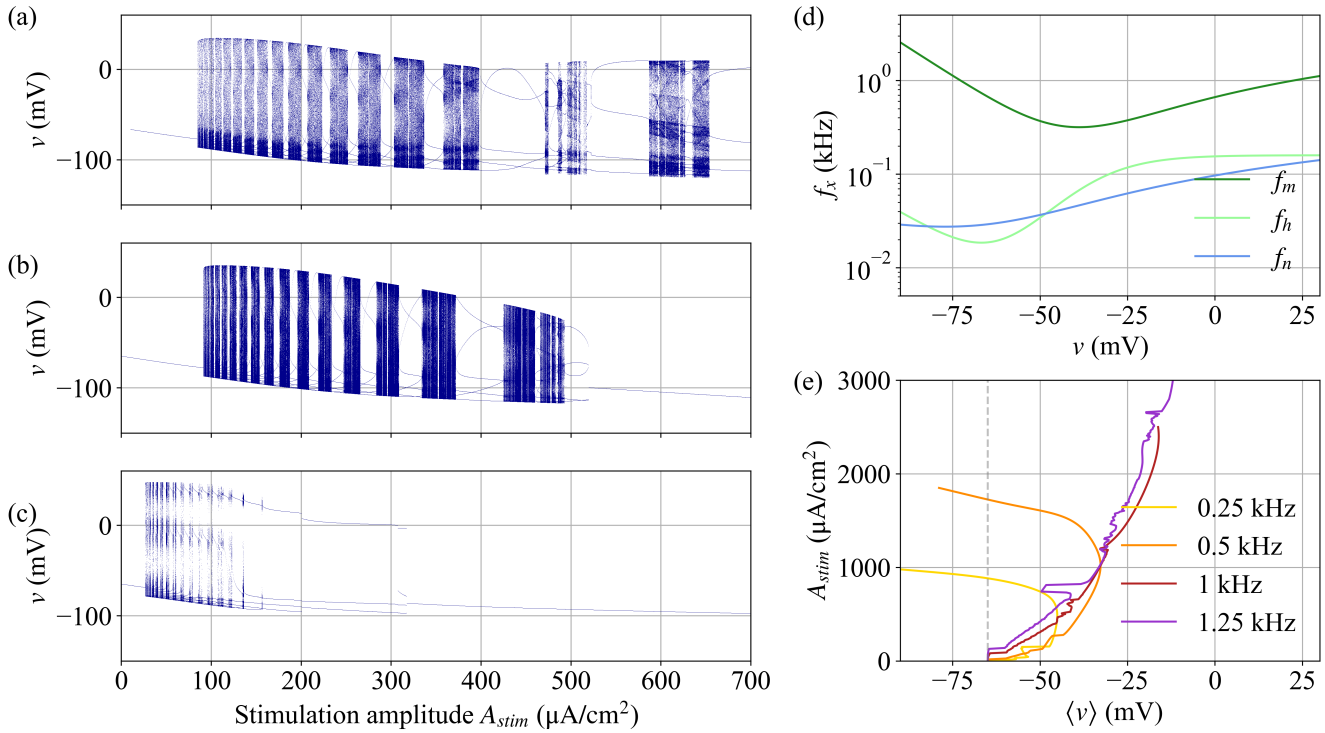


FIG. 7. Stroboscopic, frequency domain and baseline analyzes for 4D and 3D HH models. Stroboscopic bifurcation diagrams are shown for the (a) full 4D, (b) 3D $h$ reduced and (c) 3D $m$ reduced cases. In all them the forced frequency is $f_{\text{stim}} = 1$ kHz, the DC $I_0 = 0$ and the stimulation amplitude $A_{\text{stim}} \in [0, 700]\,\mu\text{A/cm}^2$. Compared to the original 4D model, the 3D $h$ maintains a similar structure of periodic/quasiperiodic successions, while for the 3D $m$ most of the quasi-periodic and chaotic-like orbits disappear. (d) The gating variable transition frequency $f_x$ (with $x$ being $m$, $h$ and $n$) as function of $v$ for the 4D HH model. Both $h$ and $n$ attain to the physiological range of frequencies, but with $m$ displaying transition frequencies in the supra-physiological regime ($f_m^{\text{min}} = 0.317$ kHz). (e) The stimulation amplitudes versus the averaged baseline membrane potential $\langle v \rangle$ for four values of the stimulation frequencies for the 4D HH model. The gray dashed line denotes the resting potential $v = -65$ mV, such that baselines to its left (right) are hyperpolarized (depolarized). For $f_{\text{stim}} = 0.25$ and 0.5 kHz the baseline shows initial depolarization but becomes hyperpolarized as $A_{\text{stim}}$ increases. For $f_{\text{stim}} = 1.0$ and 1.25 kHz, only depolarization is observed.

aimed to distinct brain regions.

Concretely, we addressed models for: (1) cortex [65], (2) hippocampus pyramidal excitatory cells [66], (3) hippocampus basket inhibitory cells [67], (4) subthalamic nucleus (STN) [68], (5) globus pallidus external (GPe) [68], and retinal ganglion cells (RGC) [69] split into two, (6) small cellular area (model I) and (7) large cellular area (model II). All them are formulated under the nonlinear conductance-based scope of the HH model, but in certain cases including new specific currents (see Appendix A 2). For DC stimulation, such models can be classified either as Type I (continuous firing-rate) or Type II (discontinuous firing-rate) [70], as detailed in Supplementary Material Section S5.

Figure 9 shows dynamical mapping for mammalian neural models, following the same procedure of Fig. 6(b) ( refer to Appendix A 4). All mappings are generated assuming a constant DC current $I_0 = 10\,\mu\text{A/cm}^2$. The stimulation frequency $f_{\text{stim}}$, vertical axis, ranges are in the regime $f_{\text{stim}} > f_{\text{osc}}^{\text{max}}$, for $f_{\text{osc}}^{\text{max}}$ the (model-specific) maximum oscillatory frequency, which also exceeds the corresponding model maximum spiking frequency $f_{\text{spk}}^{\text{max}}$. These thresholds are computed via bifurcation analysis under DC conditions and given in Supplemental Material Tab. S2 (type I models) and Tab. S3 (type II models). Maximum frequency and amplitude intervals are chosen so to capture the full diversity of dynamical trends for each model.

For such a DC current of $I_0 = 10\,\mu\text{A/cm}^2$, all models present spike at $A_{\text{stim}} = 0$. In this way, regimes for which $A_{\text{stim}} > 0$ without the presence of spiking are classified as spike-suppression (SS). Actually, SS regimes are observed in both RGC, STN, and cortical cell, but are absent in GPe and in the two hippocampal cell models. For RGCs and STN, SS occupies well-defined large portions of the parameter space, while for the cortex, it appears in a small area at the central right part of the associated map in Fig. 9. Chaotic zones arise in all cases, although they are confined to small regions in GPe and hippocampal basket models. QP and sub-harmonics ($P_k$) are ubiquitous, especially in the upper-left regions of the parameters space (high frequency, low stimulation), where induced membrane potential $A$ values are small.

Significantly, the functional mapping across models is highly diverse, with no universal pattern describing the location or arrangement of dynamical regimes. Moreover, none of the maps in Fig. 9 display any pattern similar to the original

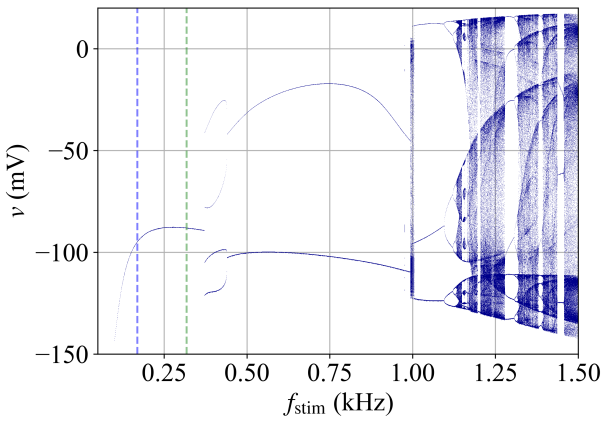


FIG. 8. Stroboscopic plot of $v$ for $f_{\text{stim}} \in [0.15, 1.5]$ kHz and a varying $A_{\text{stim}}$ accordingly to maintain constant the induced voltage amplitude $A \approx 191$ mV, Eq. (2). It shows the neural behavior when crossing the physiologic/supra-physiologic limit (blue dashed line at $f_{\text{stim}} = f_{\text{osc}}^{\max} \sim 0.169$ kHz) and the frequency for which the $m$ gating variable transition frequency is minimal (green dashed line at $f_m^{\min} = 0.317$ kHz).

HH model in Fig. 6 (b). Below we detail the specific features of each model parameter space.

Models for Cortex and Hippocampus (pyramidal and basket cells) exhibit qualitative similar responses in their parameter spaces. In all cases, the top-left region (high frequency, low amplitude) is dominated by alternating QP and high period subharmonic behavior ($P_{k>6}$). In cortical and pyramidal cell models, the central portion of the parameter space lacks a clear structure, alternating between chaotic, sub-harmonics of low period ($P_1$–$P_5$) and SS. As the induced membrane potential $A$ increases (which is equivalent to moving toward the lower right corner of the plots), both models lock into the dynamics $P_2$, similar to the usual HH. In contrast, basket hippocampal cells present a more organized structure in the parameters space central region, with alternating bands of chaotic and periodic regions. Further, as the induced membrane potential $A$ is increased, a large $P_1$ region emerges (light blue, below the white-doted line which marks $A \sim 15.1$ mV).

Despite being governed by the same conductance model (with different parameter sets, see Tab. A 2), GPe and STN display contrasting dynamical responses. The STN presents large chaotic, QP, and periodic regions, whereas the GPe predominantly shows periodic regions (computed up to $P_{200}$), with only small QP and chaotic bands. In the STN map, a clear boundary separates spiking from SS regions, indicated by a white dashed line (along which $A \sim 23$ mV). In the GPe, distinct transitions between periodic regimes are observed, nevertheless the frontiers are not characterized by clear constant values for $A$.

The RGC models I and II lead to similar structures, typified by intercalated QP and high-period subharmonic regimes at high-frequency and low stimulation amplitudes (upper-left part of the parameter space), resembling the dynamics of the cortical and hippocampal models. At lower frequencies ($1\,\text{kHz} < f_{\text{stim}} < 10\,\text{kHz}$) chaotic regions emerge embedded within periodic regimes. A large SS region occupies the central-to-upper-right portion of the parameter space, transitioning into the $P_1$ regime as the induced membrane potential $A$ increases (lower-right). Although some details of our stimulation amplitude differ from [54], the occurrence of chaotic, periodic and QP comportment at low $A_{\text{stim}}$'s is consistent with the spike-rich regime reported in [54]. Additionally, the mid region of spike suppression concurs with the suppression described in [54]. The correlation between SS regions and depolarization effects is further considered in Section III A 3.

Remarkably, unless for GPe and Basket Hippocampus, all the other models in Fig. 9 exhibit (in the parameter space) the full collection of dynamical regimes identified in the present study: SS, chaotic, quasi-periodic, and subharmonic $P_k$. Although non-spiking is absent in Fig. 9, it does arise when $I_0$ is below the spike onset threshold (see Supplemental Material, Fig. S15), hence similar to Fig. 6 for the HH model. Some models present either SS or $P_1$ for high membrane potential induced $A$ values, both behavior representing pure harmonics of the external forcing. However, they should be assumed distinct regimes, once the spiking threshold condition $m^3 h > 0.12$ is not achieved for SS. Also, if this threshold is changed, certain SS and $P_1$ regions may interchange.

We should mention that the basket hippocampal, STN and GPe models usual formulations assume the simplification $m = m_\infty(v)$. As emphasized in Section II B, this reduction might be inaccurate when $f_{\text{stim}} \gtrsim f_m$. Transition frequencies $f_x$, Eq. (4), for the gating variables of mammalian models are given in Supplemental Material, Fig. S14. For the basket hippocampal model, $f_m$ ranges from several hertz to a few kilohertz. Then, under kilohertz stimulation $f_{\text{stim}} \gtrsim f_m$ the assumption $m = m_\infty(v)$ is inaccurate, eventually resulting in loss of dynamical variability and shifts in the true locations of dynamical regimes in parameter space. For STN and GPe, $f_m(v)$ is not defined (refer to [68]), preventing extra analysis and comparison with $f_{\text{stim}}$. But these models play a significant role in computational studies of DBS and PD. Thus, our findings suggest that sodium activation dynamics should be added to STN and GPe models in order to investigate kilohertz DBS.

## III. DISCUSSION

The previous general survey sought to characterize the phenomenological behavior, mapping the dynamics of the full HH model as well as of its mammalian extensions used to describe distinct neurons under UHF stimulation. In the remaining of this work we shall discuss how our results relate to previous UHF studies and more importantly, their potential implications for neuro-modulation strategies.

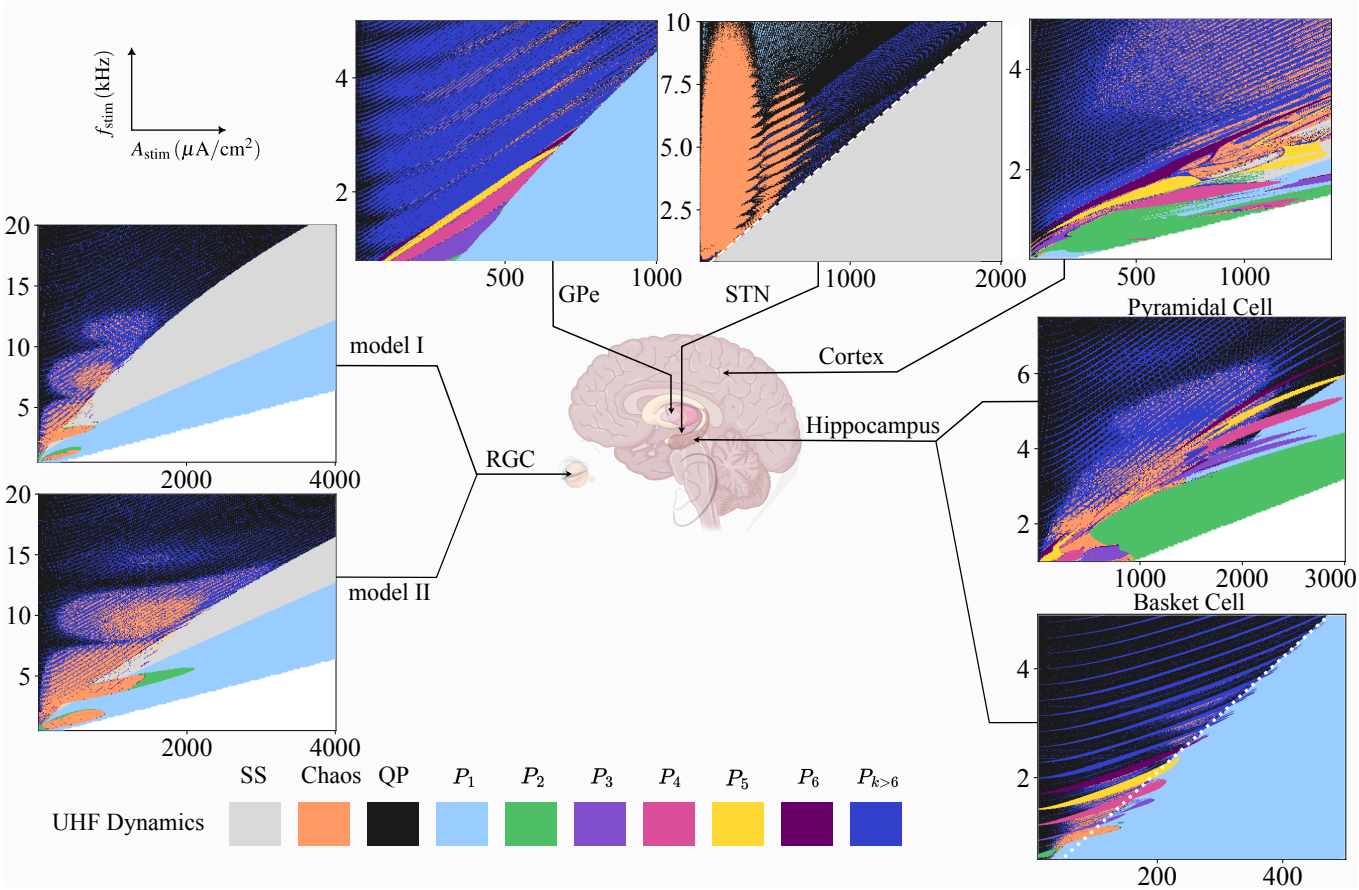


FIG. 9. Mapping of the UHF-induced stimuli dynamics of various conductance-based models in the amplitude-frequency parameter space. They address the structure of mammalian brain of: Retina (RGC), external Globus-Pallidus (GPe), SubThalamic Nucleus (STN), Cortex and Hippocampus Piramidal, and Basket. For all cases, the DC current is $I_0 = 10\,\mu\text{A/cm}^2$. The horizontal (vertical) axis displays the range of stimulation amplitude $A_{\text{stim}}$ in $\mu\text{A/cm}^2$ (stimulation frequency $f_{\text{stim}}$ in kHz). Each color represents a different dynamical behavior, namely, non-spiking (NS), chaos, quasiperiodic (QP), phase-locked ($P_1$) and sub-harmonics $P_k$ for $k = 2, 3, 4, 5, 6$ as well as higher order sub-harmonics $P_{k>6}$. White dashed (dotted) line in STN (hippocampal basket cell) map represents constant $A = 23$ mV ($A = 15.1$ mV).

## A. Comparison with previous computational and experimental studies

### 1. *Scope and limitations of theoretical approaches*

When modeling neuronal structures, two issues are key. The first is the mathematical construction itself, which ideally should represent as realistic as possible the main mechanisms regulating the neuron actual functions and responses. The second is related to the theoretical methods and simplifications assumed to treat the models (often involved, given their inherent nonlinearities). The study here points to some relevant aspects concerning these issues, as discussed below.

Our analyzes rely on biophysiologically motivated modeling, with detailed description of ionic traits, while reducing cell geometry to a point. Consequently, neural signal propagation, as studied in UHF stimulation of axons [36], falls outside the scope of our framework. Instead, we target CNS kilohertz stimulation, so to understand experimental findings [50] with macro-electrodes triggering cell populations. Of paramount importance is the fact that certain ionic channels — as the case of Na activation, see Sec. II B — are fundamental for the fast signaling processes taking place at kilohertz scales. Therefore, since nonlinear conductance-based models provide proper insight into the behavior of ionic channels, they are ideal for discussing the considered stimulus (refer to Eq. (1)).

However, conductance-based models non-linearity and high dimensionality impose significant computational demands. The inclusion of time-dependent stimulation adds further complexity, making the system non-autonomous, most likely hindering analytical solutions and investigations. In this regard, we mention averaging schemes to study non-autonomous systems [73]. In special, they are applicable to conductance-based neuronal models when two conditions are met [51]: (i) the neuron intrinsic spiking frequency under DC stimulation ($f_{\text{osc}}$) is much lower than the stimulation frequency $f_{\text{stim}}$; and (ii) the amplitude of induced membrane potential $A$ remains small compared to typical spike amplitudes ($A \ll 100$ mV). In our context, (i) is always true, as we work with supra-physiological frequencies. As for (ii), it is satisfied at low stimulation amplitudes, but might be violated

at higher values. For instance, in Fig. 3(a) both conditions hold, once for (i) $f_{osc} = 68.3\,\text{Hz} \ll f_{stim} = 1\,\text{kHz}$ and for (ii) $A = 11.9\,\text{mV} \ll 100\,\text{mV}$, so a regime well fitted for averaging techniques [51]. In contrast, in Fig. 3(d), where $A \sim 95.5\,\text{mV}$, (ii) is not verified and replacing the original by an averaged system (the premise in averaging protocols) fails. These observations show that although averaging methods are useful for revealing some of the dynamics seen under kilohertz stimulation, great caution is required to ensure that they are, in fact, suitable procedures given the parameters ranges investigated.

By the same token, dimensionality reduction or spike-resetting artifacts are commonly employed to mitigate computational complexity. Our findings support that in many instances to reduce the model dimension significantly alters the dynamics in the supra-physiological stimulation regime, e.g., see Fig. 7(a)–(c). Moreover, albeit the influence of UHF stimulation on CNS network-level dynamics has not been addressed here, natural continuations of our framework, trying to explain and characterize empirical evidences [50] pointing to positive therapeutic effects of kilohertz stimulation, should avoid reductions of fast gating variables. In particular, models based on reset conditions [74] must be avoided near stimulated population, as they fail to represent the rapid membrane dynamics essential to these phenomena.

### 2. *Possibilities of theoretically exploring biological supra-physiological parameter space*

Conductance-based neuronal models are built on physiological frequency data. Thence, an obvious question is whether they are able to reproduce dynamics in supra-physiological regimes. Remarkably, conductance-based models combined with the cable equation may accurately replicate and forecast neuronal dynamics in such a regime for PNS, providing important new understanding of phenomena related to kilohertz frequencies stimulation [40, 41, 64].

As far as we know, for CNS no prior studies have investigated membrane potential dynamics under kilohertz stimulation considering conductance-based models. While hippocampal and cortical responses have been explored experimentally [55], theoretical modeling is lacking. On the other hand, successful comparisons in retina — so called "window for the brain" [75] — between RGCs data under kilohertz stimulation and conductance-based model have been reported [54].

Here, we have provided computational predictions for RGCs and five other CNS regions under kilohertz stimulation. These results may guide future experiments needed to validate CNS conductance models in this regime. Furthermore, given the fast time scales associated with UHF, more detailed models may be necessary — e.g., incorporating stochastic ion channel behavior [29, 76].

### 3. *Correlation between depolarization and spike-suppression*

Membrane depolarization has been associated with spike-suppression in RGCs, both in simulations and experimental studies [54, 77, 78]. This suggests a possible mechanism for neural activity control. Figure 10 presents the average membrane potential variation, $\langle \Delta v \rangle = \langle v \rangle - v_0$, where $\langle v \rangle$ is the time-averaged membrane potential after filtering the external signal artifact and $v_0$ is the baseline before stimulation onset, Appendix A 3. Figure 10 (a) and (b) depict $\langle \Delta v \rangle$ for the RGC I and STN, respectively. The DC current is $I_0 = 10\,\mu\text{A/cm}^2$ (see SM Fig. S16 for HH and mammalian models). In the RGC model I, depolarized regions ($\langle \Delta v \rangle > 0$) qualitatively match the SS regions in the functional map of Fig. 9. Nonetheless, weaker levels of depolarization are also observed in the $P_1$, chaotic, and QP regimes. RGC model II displays akin results, SM Fig. S16(f). For STN in Fig. 10(b), SS occurs across a large portion of the parameter space (bellow the white dashed line in Fig. 9). But depolarization is restricted to part of this region, gradually shifting to hyperpolarization as $A$ increases.

In HH, Cortical, Pyramidal Hippocampal and GPe models (SM Figs S16(a)-(c),(e)), depolarization mostly takes place in regions of high spiking activity, such as sub-harmonics,

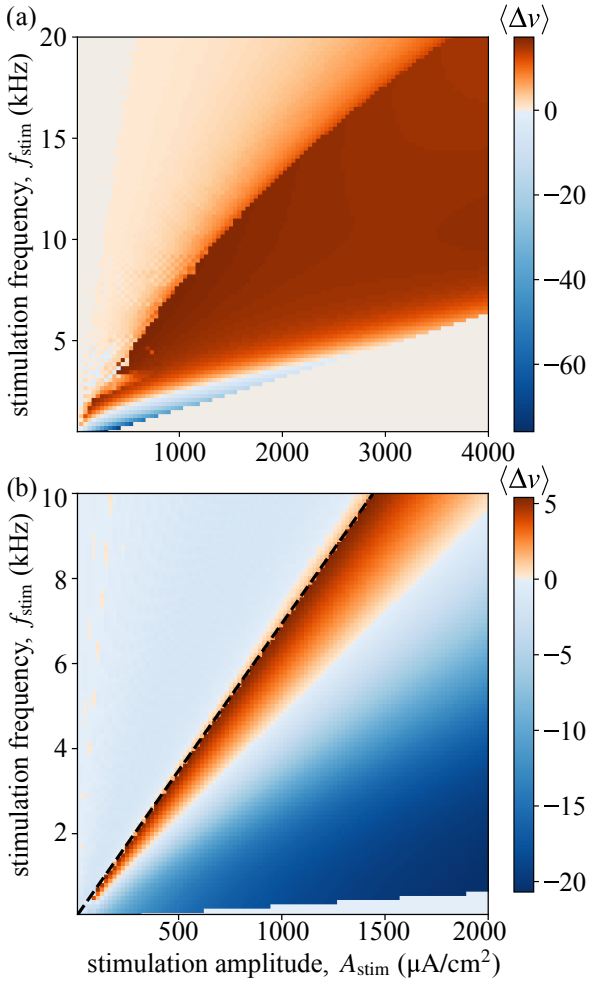


FIG. 10. Parameter space mapping of the average membrane potential shift $\langle \Delta v \rangle$ (mV) for mammalian neuronal models of (a) RGCs (model I) and (b) STN. Black dashed line in (b) marks the same value of $A = 23\,\text{mV}$ as the white dashed line in the STN functional map of Fig. 9. It divides the chaotic/QP and SS regions.

QP and chaotic. In contrast, basket hippocampal model (Fig. S16(d) in SM) shows stronger depolarization within SS regions, for $A > 15.1\,\mathrm{mV}$. These results indicate that while depolarization may contribute to SS in some neural cells, it is not an universal mechanism. We should emphasize that in [54], membrane potential dynamics were analyzed only for $I_0 = 0$ and after the filtering procedure, whereas our functional mappings (Figs. 6 and 9) consider raw, unfiltered responses.

#### 4. *Similarities between investigated dynamics and UHF stimulation of axons*

UHF stimulation of long axonal structures in the PNS elicits two main processes [36]. (i) Propagation block: axonal signal propagation is blocked near the stimulating electrode, where the stimulation current exceeds a threshold $I_{\mathrm{block}}$ [79]. The minimum frequency reported for propagation block is around 1kHz [43, 80], but with no consensus on a limiting frequency, with proposed values of up to 100 kHz [29]. (ii) Onset response: a brief asynchronous and bi-directional activity triggered when the current exceeds $I_{\mathrm{onset}}$ (usually $\leq I_{\mathrm{block}}$). This has been observed in animal experiments [40, 81] and in-silico models [41]. For motor neurons, the onset response involves an initial intense activity causing muscle twitch, followed by repetitive asynchronous activity, resulting in tetanic contractions. Although (ii) is often viewed as a limitation of UHF stimulation, it has already been used to generate controllable, biomimetic responses [82].

Parallels to (i) and (ii) above can be drawn for our CNS models. We observe large UHF-induced zones of spike suppression (either NS or SS) which somehow resemble propagation block, in the sense that synaptic inputs fail to induce spikes. This phenomenon appears in six of the eight models investigated, the exceptions are GPe and pyramidal hippocampal. Additionally, zones of aperiodic spiking activity (chaotic and QP) are observed, similarly to the onset response for axons. We conjecture that these responses could be used to control neural activity as in [82]. Nevertheless, it is still unclear whether they act in an excitatory or inhibitory (associated with desynchronization) manner. Finally, the emergence of subharmonic periodic regimes, $P_k$, is rather surprising once no clear counterpart exists in axonal UHF dynamics. Interestingly, such behavior is well known in forced nonlinear oscillators [83].

### B. Supra-physiological frequency stimulation and possibilities of concrete implementations

#### 1. *Stimulation current intensity*

Different stimulation methods are available to actually deliver supra-physiological inputs to CNS neurons. On one hand, *in vivo* and clinical neuromodulation applications rely on extracellular electrodes [84], which do not target single neurons nor uniformly affect their compartments (e.g., soma, dendrite, axon). On the other hand, intracellular current injection is a technique only feasible for *in vitro* patch clamp setups [85]. All simulations in this work assume the latter. Hence, validating our results under intracellular stimulation to extracellular setups is essential for concrete neuromodulation applications.

In extracellular stimulation, $I_{\mathrm{stim}}$ does not directly match the electrode current, it is an effective current induced by the extracellular electrical field, which decays with distance [86]. The point is that the amplitudes required to induce the various distinct dynamics observed here are considerably higher than in DC stimulation. However, recently Ref. [51] employed finite element method to show that DBS electrodes can induce local membrane currents up to $I_{\mathrm{stim}} \sim 10^4 \mu\mathrm{A/cm}^2$. This value is within the range explored in our functional dynamical maps, and concurs with stimulation levels used by [50], which reported promising UHF DBS in PD patients.

More generally, the ability to reach the required $I_{\mathrm{stim}}$ threshold for inducing UHF effects depends on the electrodes maximal charge injection. This capacity has been significantly improved through new electrode materials for neural interfaces [87]. Although the current amplitude involved in UHF regimes are systematically higher than those in conventional stimulation, they remain within the capabilities of modern stimulation systems.

#### 2. *Neuro-modulation through stimulus modulation*

Conventional neuro-modulation targets particular populations of cells, applying fixed frequency and amplitude which are either specified by the clinician or adjusted by the implant in closed-loop control setups [33]. Whether stimulation has excitatory or inhibitory effects in CNS networks is still up for debate. In fact, certain populations increase their activity, mimicking excitation, while inhibition and more complex network responses are also indirectly observed [88]. Our analyzes framework aims to classify the full diversity of responses to stimulation signals, trying to identify the conditions leading to either excitation or inhibition. This constitutes a possibility for advanced control strategies, based on tuning both frequency and amplitude within the UHF domain. We hypothesize that chosen pathways through parameter space — so to induce timed selected behaviors — could drive the network to desired, potentially nonpathological, states.

Concretely, neuro-modulation could be achieved by driving the network to proper dynamical regimes. For instance, (a) spike-suppression could block certain synaptic routes, altering network connectivity whenever necessary, (b) desynchronizing chaotic dynamics could cease a pathological condition once excessive synchronization is often associated with its emergence, (c) periodic sub-harmonics could enable synaptic propagation of external stimulation beyond the regions physically attached to electrodes (although low-pass filtering synaptic effects might limit such functioning). The maps in Figs. 6 and 9 are exactly intended to locate the distinct neural comportment in the parameter space. But in some models, e.g., standard HH, cortex and hippocampus, the transitions between distinct regimes are not sharply defined, displaying blending and mixing frontiers. Hence, the regimes boundaries might be fractal, a recurrent phenomenon in various nonlinear dy-

namical systems [89]. Thus, it is essential to disclose the mixing of different responses in the parameter space, as highly interwoven regions (possibly fractal) would lead to uncertain responses in experimental setups and the goal is to reach well defined dynamical regimes.

As previously discussed, in extracellular stimulation $f_{\text{stim}}$ remains constant, but $A_{\text{stim}}$ is position-dependent. As a result, a single-frequency arrangement can induce diverse degrees of stimulation across a network, function of the local $A_{\text{stim}}$ experienced by the neurons. Moreover, the actual neuronal response also depends on local brain morphological details. Point-neuron approximations, like ours, assume uniform stimulus, whereas more detailed models — including axonal and dendritic elements — incorporate spatially varying signals. Our analysis does not account for these aspects, which should be considered in further studies. Nevertheless, as highlighted in III A 4, the responses observed here align with those reported in axonal propagation under UHF [79–81].

### 3. *CNS responses and larger networks*

CNS neurons are, of course, embedded in networks, ranging from very local to whole brain structures. At larger scales, targeting isolated regions — although standard in clinical practices — might not be ideal in developing optimal control schemes for neurological disorders. In fact, increasing evidences suggest that no single region is solely responsible for pathologies [90]. This has motivated breakthroughs such as neurodots [91] and neural probes [92], seeking multi-zone stimulation. But their success depends on reliable models and simulation frameworks adapted to broad portions of the amplitude-frequency parameter space. Hence, it is crucial to address the effects of kilohertz in the target neuronal population and how these would drive the distinct brain structures. In addition, at shorter scales we need to understand how kilohertz-induced responses are transmitted to post-synaptic neurons so to unfold the stimulation effects on microcircuits. Actually, the ultimate goal for effective DBS therapies is to properly relate the macro and micro scales, e.g., through multiscale approaches [93]. We believe the present work represents a step forward in the characterization of the latter scale.

## ACKNOWLEDGMENTS

This study was financed in part by the Coordenação de Aperfeiçoamento de Pessoal de Nível Superior-Brazil (CAPES) - Finance Code 001 (Grant No. 88887.837508/2023-00) and from the project "Efficiency in uptake, production and distribution of photovoltaic energy distribution as well as other sources of renewable energy sources" (Grant No. 88881.311780/2018-00) via CAPES PRINT-UFPR. JGP acknowledges CAPES for a PhD scholarship (Grant No. 8887.927924/2023-00). MGELuz acknowledges CNPq-Brazil for the Research Grants No. 307512/2023-1 and No. 404577/2021-0 (Projeto Universal).

## Appendix A: Models and Methods

For the differential equations integration we have employed either the Python *scipy*-library [94] or the Julia DynamicalSystem module [95]. Bifurcation analysis has been performed using XPPAUT 8.0. The codes used for simulations and figure generation are open-source and freely available at the GitHub repository.

### 1. Hodgkin-Huxley model and dimension reduction

The Hodgkin-Huxley model [39] follows the electrical scheme presented in Fig. 1(b), where the membrane potential $v$ is governed by

$$C_m\,\dot{v} = I_{\text{stim}} - (I_{Na} + I_K + I_L), \tag{A1}$$

with $C_m = 1\,\mu\text{F}\cdot\text{cm}^{-2}$ the membrane capacitance per unit area. Moreover, $I_{Na}$, $I_K$ and $I_L$, respectively, the sodium, potassium, and leakage, currents, read

$$\begin{aligned} I_{Na} &= \overline{g}_{Na}\, m^3\, h\,(v - E_{Na}),\\ I_K &= \overline{g}_K\, n^4\,(v - E_{Na}),\\ I_L &= g_L\,(v - E_L), \end{aligned} \tag{A2}$$

where $\overline{g}_{Na} = 120\,\text{mS}\cdot\text{cm}^{-2}$, $\overline{g}_K = 36\,\text{mS}\cdot\text{cm}^{-2}$, $g_L = 0.3\,\text{mS}\cdot\text{cm}^{-2}$, $E_L = -54.387\,\text{mV}$, $E_{Na} = 50\,\text{mV}$ and $E_K = -77\,\text{mV}$.

The state of the HH model is given by $\mathbf{x} = [v, m, h, n]^T$, where $m, h, n \in [0, 1]$ are gating variables governing ion channel activation. For example, the value 1 (0) indicates fully open (closed) channel. Specifically, $m$ and $h$ control, respectively, the opening and closing of sodium channels, while $n$ controls the opening of potassium channel.

The gating dynamics follows

$$\dot{x} = \alpha_x(v)\,(1 - x) - \beta_x(v)\,x. \tag{A3}$$

Here, $x$ is either $m$, $h$ or $n$ and $\alpha_x$, $\beta_x$ are voltage-dependent transition rates derived from experimental data in [39]. In this way, we have

$$\begin{aligned} \alpha_m(v) &= 0.1\,(v + 40)/(1 - \exp[-(v + 40)/10]),\\ \beta_m(v) &= 4\,\exp[-(v + 65)/18],\\ \alpha_h(v) &= 0.07\,\exp[(v + 65)/20],\\ \beta_h(v) &= 1/(1 + \exp[-(v + 35)/10]),\\ \alpha_n(v) &= 0.01\,(v + 55)/(1 - \exp[-(v + 55)/10]),\\ \beta_n(v) &= 0.125\,\exp[-(v + 65)/80]. \end{aligned} \tag{A4}$$

From Eqs. (A3) and (A4), we define the dimensionless steady-state $x_\infty$ and the time constant $\tau_x$ (in ms) as

$$\begin{aligned} x_\infty(v) &= \frac{\alpha_x(v)}{\alpha_x(v) + \beta_x(v)},\\ \tau_x(v) &= \frac{1}{\alpha_x(v) + \beta_x(v)}. \end{aligned} \tag{A5}$$

so that Eq. (A3) can be rewritten as

$$\dot{x} = \frac{x_\infty(v) - x}{\tau_x(v)}. \tag{A6}$$

A common simplification results from $\tau_m \ll \tau_h$ and $\tau_m \ll \tau_n$. In such a regime, the system is reduced to three dimensions (3D), $\mathbf{x} = [v, h, n]^T$, by rewriting the sodium current as

$$I_{Na} = \overline{g}_{Na}\, m_\infty^3\, h\, (v - E_{Na}). \tag{A7}$$

It is called the 3D $m$ reduced model.

Another 3D reduction maintains the $m$ dynamics, but considers a linear relation between $h$ and $n$. Then, the state vector becomes $\mathbf{x} = [v, m, n]^T$, with the sodium current rewritten as

$$I_{Na} = \overline{g}_{Na}\, m^3\, (a\, n + b)\, (v - E_{Na}). \tag{A8}$$

Numerically, $a = -1.073$ and $b = 0.877$ (refer, e.g., to [61, 62]). For above one employs a least squares algorithm for the linear regression of $h$ as function of $n$, assuming a constant $I_{\text{stim}}$.

A further 2D reduction is possible by implementing two simplifications, namely, to set $m = m_\infty$ and to assume $h = an + b$, leading to $\mathbf{x} = [v,n]$ and a Na current in the form

$$I_{Na} = \overline{g}_{Na}\, m_\infty^3\, (a\, n + b)\, (v - E_{Na}). \tag{A9}$$

### 2. Models for the mammalian central nervous system

To explore the influence of UHF in a variety of locations in the mammalian central nervous system, we have considered mammalian brain models for the following regions: Basal Ganglia [68], modeling the Subthalamic Nucleus (STN) and Globus Pallidus externus (GPe); Cortex [65]; Hippocampal pyramidal excitatory [66] and basket inhibitory [67]; and finally Retinal Ganglion Cells (RGCs) [69].

In all cases, the membrane voltage $v$ obeys an expression similar to Eq. (A1), or

$$C_m\, \dot{v} = I_{\text{stim}} - \sum_{\text{ion}\in\mathcal{I}} I_{\text{ion}}, \tag{A10}$$

where $\mathcal{I}$ is the set of channels, either ionic or leakage, and $I_{\text{ion}}$ the associated current. The gating variables will depend on each specific central nervous system region. In Tab. A 2 a summary of the models is given. It presents the dimension and state vector, channels current $I_{\text{ion}}$'s equations, their conductance, reverse potential parameters, and the rates needed to describe the dynamics of auxiliary gating variables.

Almost all (see exceptions bellow) ionic currents $I_{\text{ion}}$ have the form

$$I_{\text{ion}} = \overline{g}_{\text{ion}}\, x_1^{q_1}\, x_2^{q_2}\, (v - E_{\text{ion}}), \tag{A11}$$

where $\overline{g}_{\text{ion}}$ is the membrane ionic specific conductivity in $\text{mS}\cdot\text{cm}^{-2}$, $x_1$ and $x_2$ are gating variables, $q_1,\ q_2 \geq 0$ are parameters defined for each model, and $E_{\text{ion}}$ is the ion reversal potential. The gating variable $x_i$ follows a differential equation akin to Eq. (A3). Likewise, $x_\infty\,(v)$ and $\tau_x\,(v)$ can be defined as in Eq. (A5), so that

$$\dot{x} = \phi_x\, \frac{(x_\infty(v) - x)}{\tau_x(v)}, \tag{A12}$$

with $\phi_x$ an adjustment constant, shown on Table A 2 only when $\phi_x \neq 1$.

Similarly to the original Hodgkin-Huxley model, a gating variable can be simplified, substituted by its steady-state value $x_\infty$. Such process reduces the model dimensionality and is useful in physiological frequency regime but, as shown in Sec. II B, reductions must be performed rather carefully in the supra-physiological frequency regime. Important to emphasize that the mammalian models considered in our work are exactly the same ones formulated and analyzed elsewhere. More concretely: for STN and GPe, as in [68] we set $m = m_\infty$, $a = a_\infty$, $b = b_\infty$, and $s = s_\infty$, which still leads to 5-dimensional systems; for Hippocampal inhibitory, we follow [67] and set $m = m_\infty$, reducing the model to 3D; lastly for Cortical [65], Hippocampal excitatory [66] and RGCs [69], no reductions are implemented.

Some important governing equations are not exhausted by the relations in Tab. A 2. Hence, some extra details are given below. For STN and GPe, an additional after-hiperpolarization current $I_{AHP}$, depending on the Ca concentration ($[Ca]$), is called for. It reads

$$I_{AHP} = g_{AHP}\, (v - E_K)\, \frac{[Ca]}{[Ca] + k_1}, \tag{A13}$$

where $g_{AHP} = 9\,\text{mS/cm}^2$ ($g_{AHP} = 30\,\text{mS/cm}^2$) and $k_1 = 15$ ($k_1 = 30$) for the STN (GPe) model. Moreover for STN and GPe, $[Ca]$ is modeled as

$$[\dot{Ca}] = -\epsilon\, (I_{Ca} + I_T + k_{Ca}\, [Ca]), \tag{A14}$$

with $k_{Ca} = 22.5$ ($k_{Ca} = 20$) and $\epsilon = 3.75 \cdot 10^{-5}\,\text{ms}^{-1}$ ($4 \cdot 10^{-4}\,\text{ms}^{-1}$) for STN (GPe), while $I_T$ and $I_{Ca}$ are currents in the form of Eq. (A11), as defined in Tab. A 2.

For RGCs, models I and II, the Ca reversal potential $E_{Ca}$ is not a constant, obeying

$$E_{Ca} = \frac{R\,T}{2\,F}\, \ln\left[\frac{[Ca]_e}{[Ca]_i}\right]. \tag{A15}$$

The subscripts $e$ and $i$ denote the extra- and intra-cellular spaces, with $R = 8.31451\,\text{J}\cdot\text{M}^{-1}\cdot\text{K}^{-1}$ the gas constant, $F = 9.6489 \cdot 10^4\,\text{C}$ the Faraday constant and $T$ the temperature in kelvin ($K$). We are taking $T = 308.15\,\text{K}$ ($35^oC$). For both models I and II, the extracellular calcium concentration is fixed $[Ca]_e = 0.0018M$, with the intracellular calcium concentration governed by

$$[\dot{Ca}]_i = -\frac{3\,I_{Ca}}{2\,F\,r}\,\Theta\left[-\frac{3\,I_{Ca}}{2\,F\,r}\right] - \frac{([Ca]_i - Ca_r)}{\tau_{Ca}}, \tag{A16}$$

where $r = 0.1\,\mu\text{m}$ is related to the cell surface to volume ratio, $Ca_r = 10^{-7}\,\text{M}$ is the residual calcium concentration inside the cell, $\tau_{Ca} = 1.5\,\text{ms}$ is a proper time constant, $\Theta[\,\cdot\,]$ is the Heaviside step function, and the calcium current $I_{Ca}$ is defined similarly to Eq. (A11), as shown in Tab. A 2. Finally for RGCs, the calcium-activated potassium specific conductance

is defined as

$$g_{K,Ca} = \overline{g}_{K,Ca} \frac{([Ca]_i/Ca_{\rm diss})^2}{(1+([Ca]_i/Ca_{\rm diss})^2)}, \tag{A17}$$

for $\overline{g}_{K,Ca} = 0.025\,\mathrm{mS/cm^2}$ and $Ca_{\rm diss} = 10^{-6}\,\mathrm{M}$.

Akin to the Hodgkin-Huxley, the mammalian models here can be classified as being either of type I or II [70], according to the DC current bifurcation analysis: the former exhibits a succession of saddle node points (or saddle-node homoclinic bifurcation) and can fire at arbitrarily low frequencies; whereas the latter exhibits a succession of Hopf bifurcations, firing only at a positive minimal frequency. The Supplementary Material section S5 shows the results of the bifurcation analysis for all the present models.

## 3. Numerical methods

### a. *Power spectral density*

The power spectral density (PSD) of a discrete time series $X = \{X_0, X_1, \ldots, X_{N-1}\}$, with sampling period $\Delta t$ and time duration $T = (N-1)\,\Delta t$, measures the power density at each frequency band of $X$. It is defined as

$$PSD_X(f) = \frac{\Delta t^2}{T}\,\hat{X}_f\,\hat{X}_f^* = \frac{\Delta t^2}{T}\left|\sum_{n=0}^{N-1} X_n \exp[-2\,\pi\,i\,f\,n\,\Delta t]\right|^2, \tag{A18}$$

for $\hat{X}_f$ the Fourier transform of $X$. We have calculated $\hat{X}_f$ by the Fast Fourier Transform (FFT) method [96], as implemented in the NumPy library [97]. For the membrane voltage time series $v(t)$, PSD is given in $\mathrm{mV^2 \cdot Hz^{-1}}$.

### b. *Lyapunov exponent*

The Lyapunov exponent is a fundamental quantifier to typify chaotic trajectories. A trajectory is considered chaotic if it [98]: (a) is bounded, (b) is neither periodic nor consists of equilibrium points, and (c) exhibits at least one positive Lyapunov exponent. Conditions (a) and (b) can be qualitatively identified from trajectories and bifurcation diagrams, whereas condition (c) requires measuring at least one positive exponent for the trajectory. Therefore, to calculate the maximum Lyapunov exponent (MLE) suffices.

The Lyapunov exponent characterizes the exponential rate of expansion or contraction of state space volumes around a trajectory. Suppose a $N$-dimensional dynamical system $\dot{\boldsymbol{x}} = \boldsymbol{F}(\boldsymbol{x}, \boldsymbol{p}, t)$, with $\boldsymbol{x}$ the state vector and $\boldsymbol{p}$ a set of parameters. Then, for $N$ linearly independent (LI) small perturbation vectors $\{\boldsymbol{\delta}_1, \ldots, \boldsymbol{\delta}_N\}$ around an initial condition $\boldsymbol{x}_0$, such that $\boldsymbol{x}_0 \to \boldsymbol{x}(t)$ and $\boldsymbol{x}_0 + \boldsymbol{\delta}_0 \to \boldsymbol{x}(t) + \boldsymbol{\delta}(t)$, one shall obtain

$$\boldsymbol{\delta}_i(t) \propto \exp[\lambda_i\,t]\,\boldsymbol{\delta}_i(0), \tag{A19}$$

for $t$ small enough and $i = 1, \ldots, N$, Lyapunov exponents $\lambda_1, \ldots, \lambda_N$, ordered as $\lambda_1 \geq \lambda_2 \geq \ldots \geq \lambda_N$. Thus, $\lambda_1$ is the trajectory MLE. Two algorithms are commonly used to obtain the MLE, the computationally costly but reliable QR-method and a faster and direct protocol.

The QR-method computes the full spectrum of exponents, so we just select the largest one. For an initial condition $\boldsymbol{x}_0$ and parameter values $\boldsymbol{p}$, the set of perturbation vectors $\{\boldsymbol{\delta}_1, \ldots, \boldsymbol{\delta}_N\}$ is evolved using the Jacobian $\boldsymbol{J} = d\boldsymbol{F}/d\boldsymbol{x}$ of the dynamical system. The periodic QR-decomposition ensures that perturbations remain orthonormal, preventing the alignment with the fastest expanding direction [99]. While straightforward, this approach demands significant computational time.

A faster method relies only on a single perturbation vector $\boldsymbol{\delta}_0$ around an initial $\boldsymbol{x}_0$. Then, $\boldsymbol{\delta}_0 = [\delta_0/\sqrt{N}, \ldots, \delta_0/\sqrt{N}]^T$ is a N-dimensional vector of isotropic perturbations, with norm $|\boldsymbol{\delta}_0| = \delta_0$. Two trajectories are evolved, departing from $\boldsymbol{x}_0$ and $\boldsymbol{x}_0 + \boldsymbol{\delta}_0$, during a time $t = t_0$, when the Euclidean distance $d$ between both trajectories $\boldsymbol{T}_{\boldsymbol{x}_0}(t_0)$ and $\boldsymbol{T}_{\boldsymbol{x}_0+\boldsymbol{\delta}_0}(t_0)$ escapes the limit $\delta_{\rm down} < d < \delta_{\rm up}$. The quantity $\lambda^0 = \ln[d/\delta_0]$ is recorded. The process is repeated for a new initial condition $\boldsymbol{x}_1 = \boldsymbol{T}_{\boldsymbol{x}_0}(t_0)$ and a neighboring $\boldsymbol{x}_1 + \boldsymbol{\delta}_0$, generating $\lambda^1$. The process repeats $M$ times until the total time of integration $T$ is reached. The (fast) MLE is obtained from $\lambda^{\rm fast} = T^{-1}\,\sum_i \lambda^i$. This is indeed computationally more efficient than the QR-method, but generally $\lambda^{\rm fast} \leq \lambda_1$ with $\lambda_1$ from the QR-method. This problem is enhanced in high-dimensional systems.

For the 4D HH and its lower dimensional versions, we have employed the faster method. However, for mammalian models we have found discrepancies between the two approaches for certain ranges of parameters. Hence, for mammalian models the QR-method has been used. Both have been implemented in the `ChaosTools.jl` module of the `DynamicalSystems.jl` package [100] from Julia language [101].

Along the main text, we refer to the MLE simply as $\lambda$, independent on the protocol considered. Details of the simulations setups are found in the repository [CITE].

### c. *Membrane potential averaging method*

To obtain the membrane potential average $\langle v \rangle$, we have adapted the method of [54]. First, we filter the external forcing artifact, then the entire filtered time series is averaged. The protocol starts by fitting a sinusoidal function $A\,\sin[2\,\pi\,f_{\rm stim}\,t + \phi] + A_0$ to $v(t)$. Here, $f_{\rm stim}$ and $A = A_{\rm stim}/(2\,\pi\,f_{\rm stim})$ are fixed parameters, whereas the phase $\phi$ and intercept $A_0$ are adjusted to $v(t)$ by least squares method. Then, the filtered time series results from $v_{\rm filtered}(t) = v(t) - A\,\sin[2\,\pi\,f_{\rm stim}\,t + \phi]$ for $\phi$ the fitted phase. Finally, the time series of $v_{\rm filtered}$ is divided into $N$ time steps of size $\Delta t$, so $\langle v \rangle = 1/(N\,\Delta t)\,\sum_n v_{\rm filtered}(n\,\Delta t)$.

## 4. Algorithm for behavioral mapping

To categorize the trajectories in terms of their possible dynamics, i.e., non-spiking (NS), spike-suppression (SS), chaotic, quasi-periodic (QP) and harmonics ($P_k$), we have proceed as the following. First, the MLE $\lambda$ is computed for a non-transient orbit and if $\lambda > \lambda_{\rm min}$, for $\lambda_{\rm min}$ a small threshold

| Cell Type | N. dimensions state vector | channels current equations | constants | rates |
|---|---|---|---|---|
| STN | 5<br>$\mathbf{x} = \begin{bmatrix} v \\ h \\ n \\ r \\ [Ca] \end{bmatrix}$ | $I_{Na} = \overline{g}_{Na}\, m_\infty^3 h\,(v - E_{Na})$<br>$I_K = \overline{g}_K\, n^4\,(v - E_K)$<br>$I_T = \overline{g}_T\, a_\infty^2\, b_\infty^2\,(v - E_{Ca})$<br>$I_L = g_L\,(v - E_L)$<br>$I_{Ca} = \overline{g}_{Ca}\, s_\infty^2\,(v - E_{Ca})$ | $\overline{g}_{Na} = 37.5, E_{Na} = 55$<br>$\overline{g}_K = 45, E_K = -80$<br>$\overline{g}_T = 0.5, E_{Ca} = 140$<br>$g_L = 2.25, E_L = -60$<br>$\overline{g}_{Ca} = 0.5, \phi_n = 0.75$<br>$\phi_h = 0.75, \phi_r = 0.2$ | $m_\infty = 1/(1 + \exp[-(v+30)/15]),\ s_\infty = 1/(1 + \exp[-(v+39)/8])$<br>$h_\infty = 1/(1 + \exp[(v+39)/3.1])\,,\ \tau_h = 1 + 500\,(1 + \exp[(v+57)/3])$<br>$n_\infty = 1/(1 + \exp[-(v+32)/8])\,,\ \tau_n = 1 + 100\ (1 + \exp[(v+80)/26])$<br>$r_\infty = 1/(1 + \exp[(v+67)/2])\,,\ \tau_r = 40 + 17.5\,(1 + \exp[(v-68)/2.2])$<br>$a_\infty = 1/(1 + \exp[-(v+63)/7.8])\,,$<br>$b_\infty = 1/(1 + \exp[-(r-0.4)/0.1]) - 1/(1 + \exp[4])$ |
| GPe | 5<br>$\mathbf{x} = \begin{bmatrix} v \\ h \\ n \\ r \\ [Ca] \end{bmatrix}$ | $I_{Na} = \overline{g}_{Na}\, m_\infty^3 h\,(v - E_{Na})$<br>$I_K = \overline{g}_K\, n^4\,(v - E_K)$<br>$I_T = \overline{g}_T\, a_\infty^3\, r\,(v - E_{Ca})$<br>$I_L = g_L\,(v - E_L)$<br>$I_{Ca} = \overline{g}_{Ca}\, s_\infty^2\,(v - E_{Ca})$ | $\overline{g}_{Na} = 120, E_{Na} = 55$<br>$\overline{g}_K = 30, E_K = -80$<br>$\overline{g}_T = 0.5, E_{Ca} = 120$<br>$g_L = 0.1, E_L = -55$<br>$\overline{g}_{Ca} = 0.15, \phi_n = 0.05$<br>$\phi_h = 0.05$ | $m_\infty = 1/(1 + \exp[-(v+37)/10]),\ \ s_\infty = 1/(1 + \exp[-(v+35)/2])$<br>$h_\infty = 1/(1 + \exp[(v+58)/12])\,,\ \tau_h = 0.05 + 0.27\,(1 + \exp[(v+40)/12])$<br>$n_\infty = 1/(1 + \exp[-(v+50)/14])\,,\ \tau_n = 0.05 + 0.27\ (1 + \exp[(v+40)/12])$<br>$r_\infty = 1/(1 + \exp[(v+70)/2])\,,\ \tau_r = 30,\ a_\infty = 1/(1 + \exp[-(v+57)/2])$ |
| Cortical inhibitory | 4<br>$\mathbf{x} = \begin{bmatrix} v \\ m \\ h \\ n \end{bmatrix}$ | $I_{Na} = \overline{g}_{Na}\, m^3 h\,(v - E_{Na})$<br>$I_K = \overline{g}_K n^2 (v - E_K)$<br>$I_L = g_L (v - E_L)$ | $\overline{g}_{Na} = 112, E_{Na} = 60$<br>$\overline{g}_K = 224, E_K = -90$<br>$g_L = 0.5, E_L = -70$ | $\alpha_m = 40\,(75.5 - v)/(\exp[(75.5 - v)/13.5] - 1)$<br>$\beta_m = 1.2262\ \exp[-v/42.248]$<br>$\alpha_h = 0.0035\ \exp[-v/24.186]$<br>$\beta_h = -0.017\,(v + 51.25)/(\exp[-(v + 51.25)/5.2] - 1)$<br>$\alpha_n = (95 - v)/(\exp\ [(95 - v)/11.8] - 1), \beta_n = 0.025 \exp[-v/22.222]$ |
| Hippocampal Pyramidal | 4<br>$\mathbf{x} = \begin{bmatrix} v \\ m \\ h \\ n \end{bmatrix}$ | $I_{Na} = \overline{g}_{Na}\, m^3\, h\,(v - E_{Na})$<br>$I_K = \overline{g}_K\, n^4\,(v - E_K)$<br>$I_L = g_L (v - E_L)$ | $\overline{g}_{Na} = 100, E_{Na} = 50$<br>$\overline{g}_K = 80, E_K = -100$<br>$g_L = 0.1, E_L = -67$ | $\alpha_m = 0.32\,(v + 54)\,/(1 - \exp[-(v+54)/4])\,,$<br>$\beta_m = 0.28\ (v + 27)\,/(\exp[(v+27)/5] - 1)\,,$<br>$\alpha_h = 0.128\ \exp[-(v+50)/18]\,,\ \beta_h = 4/(1 + \exp[-(v+27)/5])$<br>$\alpha_n = 0.032\ (v + 52)\,/(1 - \exp[-(v+52)/5])\,,\ \beta_n = 0.5\ \exp[-(v+57)/40]$ |
| Hippocampal Basket | 3<br>$\mathbf{x} = \begin{bmatrix} v \\ h \\ n \end{bmatrix}$ | $I_{Na} = \overline{g}_{Na}\, m_\infty^3 h\,(v - E_{Na})$<br>$I_K = \overline{g}_K\, n^4\,(v - E_K)$<br>$I_L = g_L\,(v - E_L)$ | $\overline{g}_{Na} = 35, E_{Na} = 55$<br>$\overline{g}_K = 9, E_K = -90$<br>$g_L = 0.1, E_L = -65$ | $\alpha_m = 0.1\ (v + 35)\,/(1 - \exp[-(v+35)/10])\,, \beta_m = 4\ \exp[-(v+60)/18]$<br>$\alpha_h = 0.35\ \exp[-(v+58)/20]\,, \beta_h = 5/(1 + \exp[-(v+28)/10])$<br>$\alpha_n = 0.05\ (v + 34)\,/(1 - \exp[-(v+34)/10])\,,$<br>$\beta_n = 0.625\ \exp[-(v+44)/80]$ |
| RGCs | 6<br>$\mathbf{x} = \begin{bmatrix} v \\ m \\ h \\ c \\ n \\ [Ca] \end{bmatrix}$ | $I_{Na} = \overline{g}_{Na} m^3 h (v - E_{Na})$<br>$I_K = \overline{g}_K n^4 (v - E_K)$<br>$I_{K,Ca} = \overline{g}_{K,Ca} (v - E_K)$<br>$I_{Ca} = \overline{g}_{Ca} c^3 (v - E_{Ca})$<br>$I_L = g_L (v - E_L)$ | $E_{Na} = 60.6,\ E_K = -101.34$<br>$\overline{g}_{K,Ca} = 0.025,\ g_L = 0.2$<br>$E_L = -65.02$<br>model I model II<br>$\overline{g}_{Na} = 72$ $\overline{g}_{Na} = 88.4$<br>$\overline{g}_K = 50.4$ $\overline{g}_K = 94.8$<br>$\overline{g}_{Ca} = 1.2$ $\overline{g}_{Ca} = 0.765$ | $\alpha_m = -2.725\ (v + 35)\,/(\exp[(v+35)/10] - 1)\,,$<br>$\beta_m = 90.83\ \exp[-(v+60)/20]$<br>$\alpha_h = 1.817\ \exp[-(v+52)/20]\,, \beta_h = 27.25/(1 + \exp[(v+22)/10])$<br>$\alpha_n = -0.09575\ (v + 37)\,/(\exp[-(v+37)/10] - 1)\,,$<br>$\beta_n = 1.915\ \exp[-(v+47)80]$<br>$\alpha_c = -1.362\ (v + 13)\,/(\exp[(v+13)/10] - 1)$<br>$\beta_c = 1.2262\ \exp[-v/42.248]$ |

TABLE II. The key equations and parameters values for the mammalian neuronal models considered in this work. The units are suppressed, but the conductance is in $\mathrm{mS/cm^2}$, reverse potentials in mV and time constants in ms.

(here set to $10^{-2}$), the orbit is classified as chaotic. In the case of $0 < \lambda < \lambda_{\min}$, the orbit is assumed quasi-periodic. If $\lambda < 0$, a trajectory is sampled at $1/f_{\text{stim}}$ time steps, leading to a stroboscopic orbit. Then, this orbit is tested for distinct periods $P_k$: for a stroboscopic orbit $V_{\text{strob}} = \{v_1, v_2, \dots v_N\}$, with $v_i = v(t = i/f_{\text{stim}})$, we find the orbit to be of period $k$ (so $P_k$) for $k$ the smallest integer such that $|v_n - v_{n+k}| < \epsilon$ for any $n \leq N - k$. In particular, for $k = 1$ we have checked for the presence of spikes, using the sodium channel conductance similarly to the scheme used for ISI. If the orbit is $P_1$, but there is no spike, we classify it either as NS or SS, depending on DC current behavior, otherwise it is considered $P_1$.


[1] C. W. Lynn and D. S. Bassett, The physics of brain network structure, function and control, Nature Reviews Physics **1**, 318 (2019).

[2] P. Fries, Rhythms for cognition: communication through coherence, Neuron **88**, 220 (2015).

[3] M. Thiebaut de Schotten and S. J. Forkel, The emergent properties of the connected brain, Science **378**, 505 (2022).

[4] A. Fornito, A. Zalesky, and M. Breakspear, The connectomics of brain disorders, Nature Reviews Neuroscience **16**, 159 (2015).

[5] E. S. Krames, P. H. Peckham, A. Rezai, and F. Aboelsaad, What is neuromodulation?, in *Neuromodulation* (Elsevier, 2009) pp. 3–8.

[6] A. D. Lawrence, A. H. Evans, and A. J. Lees, Compulsive use of dopamine replacement therapy in parkinson's disease: reward systems gone awry?, The Lancet Neurology **2**, 595 (2003).

[7] Y.-Y. Liu, J.-J. Slotine, and A.-L. Barabási, Controllability of complex networks, Nature **473**, 167 (2011).

[8] A. J. Whalen, S. N. Brennan, T. D. Sauer, and S. J. Schiff, Observability and controllability of nonlinear networks: The role of symmetry, Physical Review X **5**, 011005 (2015).

[9] R. Chaudhuri, B. Gerçek, B. Pandey, A. Peyrache, and I. Fiete, The intrinsic attractor manifold and population dynamics of a canonical cognitive circuit across waking and sleep, Nature neuroscience **22**, 1512 (2019).

[10] R. J. Gardner, E. Hermansen, M. Pachitariu, Y. Burak, N. A. Baas, B. A. Dunn, M.-B. Moser, and E. I. Moser, Toroidal topology of population activity in grid cells, Nature **602**, 123 (2022).

[11] M. Khona and I. R. Fiete, Attractor and integrator networks in the brain, Nature Reviews Neuroscience **23**, 744 (2022).

[12] K. Choi, W. Rosenbluth, I. R. Graf, N. Kadakia, and T. Emonet, Bifurcation enhances temporal information encoding in the olfactory periphery, PRX Life **2**, 043011 (2024).

[13] D. Durstewitz, Q. J. Huys, and G. Koppe, Psychiatric illnesses as disorders of network dynamics, Biological Psychiatry: Cognitive Neuroscience and Neuroimaging **6**, 865 (2021).

[14] M. L. Kringelbach and G. Deco, Brain states and transitions: insights from computational neuroscience, Cell Reports **32**, https://doi.org/10.1016/j.celrep.2020.108128 (2020).

[15] X. Kobeleva, P. Ritter, G. Patow, and G. Deco, Tau pathology induces whole-brain subcritical brain dynamics across the spectrum of alzheimer's disease, Alzheimer's & Dementia **18**, e064440 (2022).

[16] S. Gu, F. Pasqualetti, M. Cieslak, Q. K. Telesford, A. B. Yu, A. E. Kahn, J. D. Medaglia, J. M. Vettel, M. B. Miller, S. T. Grafton, *et al.*, Controllability of structural brain networks, Nature communications **6**, 8414 (2015).

[17] E. Tang and D. S. Bassett, Colloquium: Control of dynamics in brain networks, Reviews of modern physics **90**, 031003 (2018).

[18] E. Tang, H. Ju, G. L. Baum, D. R. Roalf, T. D. Satterthwaite, F. Pasqualetti, and D. S. Bassett, Control of brain network dynamics across diverse scales of space and time, Physical Review E **101**, 062301 (2020).

[19] J. D. Touboul, C. Piette, L. Venance, and G. B. Ermentrout, Noise-induced synchronization and antiresonance in interacting excitable systems: applications to deep brain stimulation in parkinson's disease, Physical Review X **10**, 011073 (2020).

[20] J. K. Krauss, N. Lipsman, T. Aziz, A. Boutet, P. Brown, J. W. Chang, B. Davidson, W. M. Grill, M. I. Hariz, A. Horn, *et al.*, Technology of deep brain stimulation: current status and future directions, Nature Reviews Neurology **17**, 75 (2021).

[21] M. Popova, C. C. Hilgetag, and M.-T. Hütt, Perturbation therapies for neurodegenerative disorders: How attractors of excitable networks can help, Physical Review E **110**, 054406 (2024).

[22] M. Lucas, J. Newman, and A. Stefanovska, Stabilization of dynamics of oscillatory systems by nonautonomous perturbation, Physical Review E **97**, 042209 (2018).

[23] P. A. Tass, L. Qin, C. Hauptmann, S. Dovero, E. Bezard, T. Boraud, and W. G. Meissner, Coordinated reset has sustained aftereffects in parkinsonian monkeys, Annals of neurology **72**, 816 (2012).

[24] J. Wang, S. Nebeck, A. Muralidharan, M. D. Johnson, J. L. Vitek, and K. B. Baker, Coordinated reset deep brain stimulation of subthalamic nucleus produces long-lasting, dose-dependent motor improvements in the 1-methyl-4-phenyl-1, 2, 3, 6-tetrahydropyridine non-human primate model of parkinsonism, Brain stimulation **9**, 609 (2016).

[25] R. Rokyta and J. Fricová, Neurostimulation methods in the treatment of chronic pain, Physiological research **61**, S23 (2012).

[26] J. D. Weiland and M. S. Humayun, Visual prosthesis, Proceedings of the IEEE **96**, 1076 (2008).

[27] S. J. Bensmaia, D. J. Tyler, and S. Micera, Restoration of sensory information via bionic hands, Nature Biomedical Engineering **7**, 443 (2023).

[28] J. Frey, J. Cagle, K. A. Johnson, J. K. Wong, J. D. Hilliard, C. R. Butson, M. S. Okun, and C. de Hemptinne, Past, present, and future of deep brain stimulation: hardware, software, imaging, physiology and novel approaches, Frontiers in neurology **13**, 825178 (2022).

[29] C. Neudorfer, C. T. Chow, A. Boutet, A. Loh, J. Germann, G. J. Elias, W. D. Hutchison, and A. M. Lozano, Kilohertz-frequency stimulation of the nervous system: A review of underlying mechanisms, Brain Stimulation: Basic, Translational, and Clinical Research in Neuromodulation **14**, 513 (2021).

[30] P. Limousin, P. Pollak, A. Benazzouz, D. Hoffmann, J.-F. Le Bas, J. Perret, A. Benabid, and E. Broussolle, Effect on parkinsonian signs and symptoms of bilateral subthalamic nucleus stimulation, The Lancet **345**, 91 (1995).

[31] N. Li, J. C. Baldermann, A. Kibleur, S. Treu, H. Akram, G. J. Elias, A. Boutet, A. M. Lozano, B. Al-Fatly, B. Strange, *et al.*, A unified connectomic target for deep brain stimulation in obsessive-compulsive disorder, Nature communications **11**,

3364 (2020).

[32] A. S. Ríos, S. Oxenford, C. Neudorfer, K. Butenko, N. Li, N. Rajamani, A. Boutet, G. J. Elias, J. Germann, A. Loh, *et al.*, Optimal deep brain stimulation sites and networks for stimulation of the fornix in alzheimer's disease, Nature communications **13**, 7707 (2022).

[33] A. M. Lozano, N. Lipsman, H. Bergman, P. Brown, S. Chabardes, J. W. Chang, K. Matthews, C. C. McIntyre, T. E. Schlaepfer, M. Schulder, *et al.*, Deep brain stimulation: current challenges and future directions, Nature Reviews Neurology **15**, 148 (2019).

[34] W.-J. Neumann, R. Gilron, S. Little, and G. Tinkhauser, Adaptive deep brain stimulation: from experimental evidence toward practical implementation, Movement disorders **38**, 937 (2023).

[35] M. Tosato, K. Yoshida, E. Toft, and J. Struijk, Quasi-trapezoidal pulses to selectively block the activation of intrinsic laryngeal muscles during vagal nerve stimulation, Journal of neural engineering **4**, 205 (2007).

[36] Y. A. Patel and R. J. Butera, Challenges associated with nerve conduction block using kilohertz electrical stimulation, Journal of neural engineering **15**, 031002 (2018).

[37] A. Soin, Z.-P. Fang, and J. Velasco, Peripheral neuromodulation to treat postamputation pain, Stimulation of the Peripheral Nervous System **29**, 158 (2016).

[38] G. Yi and W. M. Grill, Kilohertz waveforms optimized to produce closed-state na+ channel inactivation eliminate onset response in nerve conduction block, PLoS computational biology **16**, e1007766 (2020).

[39] A. L. Hodgkin and A. F. Huxley, A quantitative description of membrane current and its application to conduction and excitation in nerve, The Journal of physiology **117**, 500 (1952).

[40] K. L. Kilgore and N. Bhadra, Nerve conduction block utilising high-frequency alternating current, Medical and Biological Engineering and Computing **42**, 394 (2004).

[41] N. Bhadra, E. A. Lahowetz, S. T. Foldes, and K. L. Kilgore, Simulation of high-frequency sinusoidal electrical block of mammalian myelinated axons, Journal of computational neuroscience **22**, 313 (2007).

[42] M. H. Negm and I. C. Bruce, The effects of hcn and klt ion channels on adaptation and refractoriness in a stochastic auditory nerve model, IEEE Transactions on Biomedical Engineering **61**, 2749 (2014).

[43] N. Bhadra and K. L. Kilgore, High-frequency electrical conduction block of mammalian peripheral motor nerve, Muscle & Nerve: Official Journal of the American Association of Electrodiagnostic Medicine **32**, 782 (2005).

[44] C. Tai, J. R. Roppolo, and W. C. de GROAT, Response of external urethral sphincter to high frequency biphasic electrical stimulation of pudendal nerve, The Journal of urology **174**, 782 (2005).

[45] N. Bhadra, E. L. Foldes, D. M. Ackermann, and K. L. Kilgore, Reduction of the onset response in high frequency nerve block with amplitude ramps from non-zero amplitudes, in *2009 Annual International Conference of the IEEE Engineering in Medicine and Biology Society* (IEEE, 2009) pp. 650–653.

[46] N. Pelot and W. Grill, In vivo quantification of excitation and kilohertz frequency block of the rat vagus nerve, Journal of neural engineering **17**, 026005 (2020).

[47] A. L. Benabid, P. Pollak, D. Hoffmann, C. Gervason, M. Hommel, J. Perret, J. De Rougemont, and D. Gao, Long-term suppression of tremor by chronic stimulation of the ventral intermediate thalamic nucleus, The Lancet **337**, 403 (1991).

[48] J. Couto and W. M. Grill, Kilohertz frequency deep brain stimulation is ineffective at regularizing the firing of model thalamic neurons, Frontiers in computational neuroscience **10**, 22 (2016).

[49] B. Hutcheon and Y. Yarom, Resonance, oscillation and the intrinsic frequency preferences of neurons, Trends in neurosciences **23**, 216 (2000).

[50] I. E. Harmsen, D. J. Lee, R. F. Dallapiazza, P. De Vloo, R. Chen, A. Fasano, S. K. Kalia, M. Hodaie, and A. M. Lozano, Ultra-high-frequency deep brain stimulation at 10,000 Hz improves motor function, Movement Disorders **34**, 146 (2019).

[51] K. Pyragas, V. Novičenko, and P. A. Tass, Mechanism of suppression of sustained neuronal spiking under high-frequency stimulation, Biological Cybernetics **107**, 669 (2013).

[52] S. V. Karnup, W. De Groat, J. Beckel, and C. Tai, Effect of biphasic khz field stimulation on ca1 pyramidal neurons in slices, Medical Research Archives **10**, https://doi.org/10.18103/mra.v10i8.2957 (2022).

[53] L. S. Lesperance, M. Lankarany, T. C. Zhang, R. Esteller, S. Ratté, and S. A. Prescott, Artifactual hyperpolarization during extracellular electrical stimulation: Proposed mechanism of high-rate neuromodulation disproved, Brain stimulation **11**, 582 (2018).

[54] J.-I. Lee, P. Werginz, T. Kameneva, M. Im, and S. I. Fried, Membrane depolarization mediates both the inhibition of neural activity and cell-type-differences in response to high-frequency stimulation, Communications Biology **7**, 734 (2024).

[55] C. R. Ravasio, K. Kondabolu, S. Zhou, E. Lowet, E. San Antonio, R. A. Mount, S. K. Bhogal, and X. Han, Kilohertz electrical stimulation evokes robust cellular responses like conventional frequencies but distinct population dynamics, Communications Biology **8**, 1 (2025).

[56] B. Hassard, Bifurcation of periodic solutions of the hodgkin-huxley model for the squid giant axon, Journal of Theoretical Biology **71**, 401 (1978).

[57] I. S. Labouriau, Degenerate hopf bifurcation and nerve impulse, SIAM journal on mathematical analysis **16**, 1121 (1985).

[58] J. Guckenheimer and J. Labouriau, Bifurcation of the hodgkin and huxley equations: a new twist, Bulletin of Mathematical Biology **55**, 937 (1993).

[59] H. Fukai, T. Nomura, S. Doi, and S. Sato, Hopf bifurcations in multiple-parameter space of the hodgkin-huxley equations ii. singularity theoretic approach and highly degenerate bifurcations, Biological Cybernetics **82**, 223 (2000).

[60] B. A. y Arcas, A. L. Fairhall, and W. Bialek, Computation in a single neuron: Hodgkin and huxley revisited, Neural computation **15**, 1715 (2003).

[61] T. B. Kepler, L. Abbott, and E. Marder, Reduction of conductance-based neuron models, Biological cybernetics **66**, 381 (1992).

[62] C. Meunier, Two and three dimensional reductions of the hodgkin-huxley system: separation of time scales and bifurcation schemes, Biological cybernetics **67**, 461 (1992).

[63] B. Ermentrout, Reduction of conductance-based models with slow synapses to neural nets, Neural Computation **6**, 679 (1994).

[64] D. M. Ackermann, N. Bhadra, M. Gerges, and P. J. Thomas, Dynamics and sensitivity analysis of high-frequency conduction block, Journal of neural engineering **8**, 065007 (2011).

[65] A. Erisir, D. Lau, B. Rudy, and C. S. Leonard, Function of specific k+ channels in sustained high-frequency firing of fast-spiking neocortical interneurons, Journal of neurophysiology **82**, 2476 (1999).

[66] R. D. Traub and R. Miles, *Neuronal networks of the hippocampus*, Vol. 777 (Cambridge University Press, 1991).

[67] X.-J. Wang and G. Buzsáki, Gamma oscillation by synaptic inhibition in a hippocampal interneuronal network model, Journal of neuroscience **16**, 6402 (1996).

[68] D. Terman, J. E. Rubin, A. Yew, and C. Wilson, Activity patterns in a model for the subthalamopallidal network of the basal ganglia, Journal of Neuroscience **22**, 2963 (2002).

[69] J. F. Fohlmeister, E. D. Cohen, and E. A. Newman, Mechanisms and distribution of ion channels in retinal ganglion cells: using temperature as an independent variable, Journal of neurophysiology **103**, 1357 (2010).

[70] B. Ermentrout and D. H. Terman, *Mathematical foundations of neuroscience*, Vol. 35 (Springer, 2010).

[71] H. Sakaguchi and K. Yamasaki, Suppression and frequency control of repetitive spiking in the FitzHugh-Nagumo model, Physical Review E **108**, 014207 (2023).

[72] S. H. Strogatz, *Nonlinear dynamics and chaos: with applications to physics, biology, chemistry, and engineering* (CRC press, 2018).

[73] J. A. Sanders, F. Verhulst, and J. Murdock, *Averaging methods in nonlinear dynamical systems*, Vol. 59 (Springer, 2007).

[74] E. M. Izhikevich, Resonate-and-fire neurons, Neural networks **14**, 883 (2001).

[75] A. London, I. Benhar, and M. Schwartz, The retina as a window to the brain—from eye research to cns disorders, Nature Reviews Neurology **9**, 44 (2013).

[76] J. A. White, J. T. Rubinstein, and A. R. Kay, Channel noise in neurons, Trends in neurosciences **23**, 131 (2000).

[77] T. Kameneva, M. Maturana, A. Hadjinicolaou, S. Cloherty, M. Ibbotson, D. Grayden, A. Burkitt, and H. Meffin, Retinal ganglion cells: mechanisms underlying depolarization block and differential responses to high frequency electrical stimulation of on and off cells, Journal of neural engineering **13**, 016017 (2016).

[78] T. Guo, D. Tsai, C. Y. Yang, A. Al Abed, P. Twyford, S. I. Fried, J. W. Morley, G. J. Suaning, S. Dokos, and N. H. Lovell, Mediating retinal ganglion cell spike rates using high-frequency electrical stimulation, Frontiers in neuroscience **13**, 413 (2019).

[79] K. L. Kilgore and N. Bhadra, Reversible nerve conduction block using kilohertz frequency alternating current, Neuromodulation: Technology at the Neural Interface **17**, 242 (2014).

[80] R. P. Williamson and B. J. Andrews, Localized electrical nerve blocking, IEEE Transactions on Biomedical Engineering **52**, 362 (2005).

[81] B. R. Bowman and D. R. McNeal, Response of single alpha motoneurons to high-frequency pulse trains: firing behavior and conduction block phenomenon, Stereotactic and Functional Neurosurgery **49**, 121 (1986).

[82] E. Formento, E. D'Anna, S. Gribi, S. P. Lacour, and S. Micera, A biomimetic electrical stimulation strategy to induce asynchronous stochastic neural activity, Journal of neural engineering **17**, 046019 (2020).

[83] C. Hayashi, *Nonlinear oscillations in physical systems* (Princeton University Press, 2014).

[84] A. M. Lozano and M. Hallett, *Brain stimulation* (Newnes, 2013).

[85] E. Neher and B. Sakmann, The patch clamp technique, Scientific American **266**, 44 (1992).

[86] F. Rattay, The basic mechanism for the electrical stimulation of the nervous system, Neuroscience **89**, 335 (1999).

[87] N. Wu, S. Wan, S. Su, H. Huang, G. Dou, and L. Sun, Electrode materials for brain–machine interface: A review, InfoMat **3**, 1174 (2021).

[88] S. Chiken and A. Nambu, Mechanism of deep brain stimulation: inhibition, excitation, or disruption?, The neuroscientist **22**, 313 (2016).

[89] J. Aguirre, R. L. Viana, and M. A. Sanjuán, Fractal structures in nonlinear dynamics, Reviews of Modern Physics **81**, 333 (2009).

[90] Z. Sha, T. D. Wager, A. Mechelli, and Y. He, Common dysfunction of large-scale neurocognitive networks across psychiatric disorders, Biological psychiatry **85**, 379 (2019).

[91] D. De Ridder, M. A. Siddiqi, J. Dauwels, W. A. Serdijn, and C. Strydis, Neurodots: From single-target to brain-network modulation: Why and what is needed?, Neuromodulation: Technology at the Neural Interface https://doi.org/10.1016/j.neurom.2024.01.003 (2024).

[92] Y.-G. Park, Y. W. Kwon, C. S. Koh, E. Kim, D. H. Lee, S. Kim, J. Mun, Y.-M. Hong, S. Lee, J.-Y. Kim, *et al.*, In-vivo integration of soft neural probes through high-resolution printing of liquid electronics on the cranium, Nature communications **15**, 1772 (2024).

[93] J. M. Meier, D. Perdikis, A. Blickensdörfer, L. Stefanovski, Q. Liu, O. Maith, H. Ü. Dinkelbach, J. Baladron, F. H. Hamker, and P. Ritter, Virtual deep brain stimulation: Multiscale co-simulation of a spiking basal ganglia model and a whole-brain mean-field model with the virtual brain, Experimental Neurology **354**, 114111 (2022).

[94] P. Virtanen, R. Gommers, T. E. Oliphant, M. Haberland, T. Reddy, D. Cournapeau, E. Burovski, P. Peterson, W. Weckesser, J. Bright, S. J. van der Walt, M. Brett, J. Wilson, K. J. Millman, N. Mayorov, A. R. J. Nelson, E. Jones, R. Kern, E. Larson, C. J. Carey, İ. Polat, Y. Feng, E. W. Moore, J. VanderPlas, D. Laxalde, J. Perktold, R. Cimrman, I. Henriksen, E. A. Quintero, C. R. Harris, A. M. Archibald, A. H. Ribeiro, F. Pedregosa, P. van Mulbregt, and SciPy 1.0 Contributors, SciPy 1.0: Fundamental Algorithms for Scientific Computing in Python, Nature Methods **17**, 261 (2020).

[95] G. Datseris, Dynamicalsystems.jl: A julia software library for chaos and nonlinear dynamics, Journal of Open Source Software **3**, 598 (2018).

[96] J. W. Cooley and J. W. Tukey, An algorithm for the machine calculation of complex fourier series, Mathematics of computation **19**, 297 (1965).

[97] C. R. Harris, K. J. Millman, S. J. van der Walt, R. Gommers, P. Virtanen, D. Cournapeau, E. Wieser, J. Taylor, S. Berg, N. J. Smith, R. Kern, M. Picus, S. Hoyer, M. H. van Kerkwijk, M. Brett, A. Haldane, J. F. del Río, M. Wiebe, P. Peterson, P. Gérard-Marchant, K. Sheppard, T. Reddy, W. Weckesser, H. Abbasi, C. Gohlke, and T. E. Oliphant, Array programming with NumPy, Nature **585**, 357 (2020).

[98] K. T. Alligood, T. D. Sauer, J. A. Yorke, and D. Chillingworth, Chaos: an introduction to dynamical systems, SIAM Review **40**, 732 (1998).

[99] G. Datseris and U. Parlitz, *Nonlinear dynamics: a concise introduction interlaced with code* (Springer Nature, 2022).

[100] G. Datseris, Dynamicalsystems. jl: A julia software library for chaos and nonlinear dynamics, Journal of Open Source Software **3**, 598 (2018).

[101] J. Bezanson, A. Edelman, S. Karpinski, and V. B. Shah, Julia: A fresh approach to numerical computing, SIAM review **59**, 65 (2017).